Phenomenology of a 96 GeV Higgs boson in the 2HDM with an additional singlet

S. Heinemeyer[1,*] C. Li,[2,†] F. Lika,[3,‡] G. Moortgat-Pick,[2,3,§] and S. Paasch[2,∥]

[1]*Instituto de Física Teórica (UAM/CSIC), Universidad Autónoma de Madrid,*
Cantoblanco, 28049 Madrid, Spain
[2]*Deutsches Elektronen-Synchrotron DESY, Notkestraße 85, 22607 Hamburg, Germany*
[3]*II. Institut für Theoretische Physik, Universität Hamburg,*
Luruper Chaussee 149, 22761 Hamburg, Germany

We discuss a $\sim 3\sigma$ signal (local) in the light Higgs-boson search in the diphoton decay mode at ~ 96 GeV as reported by CMS, together with a $\sim 2\sigma$ excess (local) in the $b\bar{b}$ final state at the Large Electron Positron Collider (LEP) in the same mass range. We interpret this possible signal as a Higgs boson in the 2 Higgs doublet model type II with an additional Higgs singlet, which can be either complex (2HDMS) or real (N2HDM), where the 2HDMS so far has never been analyzed as an explanation of these excesses. An emphasis of our work is the differences between and the possible distinction of the two models in this context. We find that the lightest $\mathcal{CP}$-even Higgs boson of the two models can equally yield a perfect fit to both excesses simultaneously, while the second lightest state is in full agreement with the Higgs-boson measurements at 125 GeV, and the full Higgs-boson sector is in agreement with all Higgs exclusion bounds from LEP, the Tevatron and the LHC as well as other theoretical and experimental constraints. We derive bounds on the 2HDMS and N2HDM Higgs sectors from a fit to both excesses and describe how this signal can be further analyzed at future e^+e^- colliders, such as the International Linear Collider (ILC). We analyze in detail the anticipated precision of the coupling measurements of the 96 GeV Higgs boson at the ILC. We find that these Higgs-boson measurements at the LHC and the ILC cannot distinguish between the two Higgs-sector realizations.

I. INTRODUCTION

In the year 2012 the ATLAS and CMS collaborations discovered a new particle that is—within theoretical and experimental uncertainties—consistent with the existence of a Higgs boson as predicted by the Standard Model (SM) with a mass of ~ 125 GeV [1–3]. So far no conclusive signs of physics beyond the SM (BSM) have been found at the LHC. However, the measurements of Higgs-boson production and decay rates at the LHC, which are known experimentally to a precision of roughly $\sim 10\%$–20%, leave ample room for BSM interpretations. Many BSM models contain extended Higgs-boson sectors. Consequently, one of the main tasks of the LHC run III and beyond is to

determine whether the observed scalar boson forms part of the Higgs-boson sector of an extended model. Such extended Higgs-boson sectors naturally possess additional Higgs bosons, which can have masses larger, but also smaller, than 125 GeV. Some examples for the latter can be found in Refs. [4–8] (see also the discussion below). Therefore, the search for lighter Higgs bosons forms an important part in the BSM Higgs-boson program at the (HL-)LHC and planned lepton collider experiments.

Searches for Higgs bosons below 125 GeV have been performed at the large electron positron (LEP) collider [9–11], the Tevatron [12] and the LHC [13–16]. LEP observed a 2.3σ local excess observed in the $e^+e^- \to Z(H \to b\bar{b})$ channel [10], consistent with a scalar of mass ~ 98 GeV. However, due to the $b\bar{b}$ final state the mass resolution is rather coarse. ATLAS and CMS searched for light Higgs bosons in the diphoton final state. The CMS Run II results [14] show a local excess of $\sim 3\sigma$ at ~ 96 GeV, where a similar excess of 2σ had been observed in Run I [17] at roughly the same mass. First Run II results from ATLAS, on the other hand, using 80 fb^{-1} turned out to be weaker than the corresponding CMS results, see, e.g., Fig. 1 in Ref. [18].

Since the CMS and the LEP excesses in the searches for light Higgs-bosons are found effectively at the same mass,

*Sven.Heinemeyer@cern.ch
†cheng.li@desy.de
‡florian.lika@desy.de
§gudrid.moortgat-pick@desy.de
∥steven.paasch@desy.de

the question arises whether they have a common origin, i.e. which model can accommodate them simultaneously, while being in agreement with all other Higgs-boson related limits and measurements. The two excesses have been described in the following models (see also [18–21]): (i) the next-to-two Higgs doublet model, N2HDM [21–26], as will be discussed below (additionally simultaneous explanations for possible excesses at ∼400 GeV are discussed in Ref. [26]); (ii) various realizations of the next-to-minimal supersymmetric SM, NMSSM [26–28] (see also Ref. [26] for the possible ∼400 GeV excesses); (iii) the μ-from-ν supersymmetric SM ($\mu\nu$SSM) with one [29] and three generations [30] of right-handed neutrinos; (iv) Higgs inflation inspired μNMSSM [31]; (v) NMSSM with a seesaw extension [32]; (vi) Higgs singlet with additional vectorlike matter, as well as two Higgs doublet model, 2HDM type I [33]; (vii) 2HDM type I with a moderately to-strongly fermiophobic *CP*-even Higgs [34]; (viii) 2HDM type II extended by a complex singlet, obeying an additional $U(1)$ symmetry, such that the imaginary part of the singlet is a dark matter candidate [35]; (ix) radion model [36]; (x) Higgs associated with the breakdown of an $U(1)_{L_\mu L_\tau}$ symmetry [37]; (xi) minimal dilaton model [38]; (xii) composite framework containing a pseudo-Nambu Goldstone-type light scalar [20]; (xiii) SM extended by a complex singlet scalar field (which can also accommodate a pseudo-Nambu Goldstone dark matter) [39]; and (xiv) anomaly free $U(1)'$ extensions of SM with two complex scalar singlets [40]. In the model realizations (xiii) and (xiv) the required diphoton decay rate is reached by adding additional charged particles that couple to the 96 GeV scalar. On the other hand, in the MSSM the CMS excess cannot be realized [8]. The important question arises, how one can distinguish the various model realizations, in particular when they are similar to each other, e.g., the various 2HDM extensions or the supersymmetric (SUSY) realizations. In this article we take a first step in this direction and focus on the distinction of two models describing the two excesses.

In this paper we focus on pure Higgs-sector extensions of the SM, based on the 2HDM type II (which naturally lead the way to SUSY realizations). As listed above, the 2HDM with an additional real singlet, the N2HDM can describe simultaneously the LEP and CMS excesses at ∼96 GeV [22]. While this model possesses an additional real Higgs singlet, it also has an additional $\mathbb{Z}_2$ symmetry that can provide a dark matter candidate in the case of a zero singlet vev [41–43]. Such an additional $\mathbb{Z}_2$ symmetry, however, is not compatible with the Higgs sector of supersymmetric models, such as the NMSSM (which can equally describe the two excesses [27,28]). The "pure Higgs sector extension" of the NMSSM is the 2HDM with an additional complex singlet and an additional $\mathbb{Z}_3$ symmetry, the 2HDMS. It should be noted that our study contains, to our knowledge, the first phenomenological analysis of the 2HDMS with the $\mathbb{Z}_3$ symmetry applied. Previous studies focused on the model without enforcing the $\mathbb{Z}_3$ symmetry [44,45] (and did not analyze the 96 GeV excesses).

In this article, for the first time we attempt to discriminate models explaining the excesses at 96 GeV. We analyze for which part of the parameter spaces the 2HDMS and N2HDM (type II) can describe the CMS and LEP excesses. We investigate where the models give the same predictions, where they may differ, and how the two model realizations could possibly be distinguished from each other.

For the analyses of the 2HDMS and N2HDM Higgs-boson sectors at future colliders we employ the anticipated reach and precision of the HL-LHC, and furthermore of a possible future e^+e^- collider, where we focus on the International Linear Collider (ILC) with a center-of-mass energy of $\sqrt{s} = 250$ GeV (ILC250). In particular we show what can be learned from a measurement of the couplings of the 125 GeV Higgs boson at the ILC250. Going one step further, we present for the first time a phenomenological analysis of the new state at ∼96 GeV at the ILC250: we analyze to which precision its couplings can be measured at the ILC250 and what can be learned from these future measurements about the underlying model. We include all relevant technical details for such a coupling measurement of a light Higgs boson at the ILC250.

Our paper is organized as follows. In Sec. II we describe the relevant features of the 2HDMS and the N2HDM, and where they differ from each other. The experimental and theoretical constraints taken into account are given in Sec. III. Details about the experimental excesses at CMS and LEP, as well as details on their implementations, are discussed in Sec. IV. In Sec. V we present our results in the 2HDMS and contrast them to the results in the N2HDM. We discuss the possibilities to investigate these scenarios at the HL-LHC and the ILC250, including an analysis of the coupling measurement of the new state at ∼96 GeV at the ILC250. We conclude with Sec. VI. In Appendix A we provide further details on the two models, while in Appendix B we provide all technical details for the coupling measurement of a light Higgs boson at the ILC250.

II. THE N2HDM AND THE 2HDMS

In this section we provide a description of the two models under consideration. We emphasize the similarities, but in particular also the differences of the two models, and briefly discuss how they could manifest themselves in phenomenological analyses.

A. Symmetries and the Higgs potential

In this section we define the two models under consideration, the N2HDM and the 2HDMS. Both extend the 2HDM with the doublets Φ_1 and Φ_2 by a singlet S, which is taken to be real (complex) for the N2HDM (2HDMS). After electroweak symmetry breaking, the scalar component of Φ_1, Φ_2, and S acquire the nontrivial vacuum expectation values (vevs). Thus the fields can be expanded around the vevs and have the following expressions:

$$\Phi_1 = \begin{pmatrix} \chi_1^+ \\ \phi_1 \end{pmatrix} = \begin{pmatrix} \chi_1^+ \\ v_1 + \frac{\rho_1 + i\eta_1}{\sqrt{2}} \end{pmatrix} \Phi_2 = \begin{pmatrix} \chi_2^+ \\ \phi_2 \end{pmatrix}$$

$$= \begin{pmatrix} \chi_2^+ \\ v_2 + \frac{\rho_2 + i\eta_2}{\sqrt{2}} \end{pmatrix} \quad S = v_S + \frac{\rho_S + i\eta_S}{\sqrt{2}}, \quad (1)$$

where the η_S is absent in the N2HDM.

The models furthermore differ by their symmetry structures. Both models obey the $\mathbb{Z}_2$ symmetry that is imposed already on the 2HDM to avoid flavor-changing neutral currents at tree level (where we will focus on "type II," see the discussion below). Concerning the singlet in the N2HDM, it is odd under an additional $\mathbb{Z}_2'$ symmetry. The 2HDMS, on the other hand, obeys an additional $\mathbb{Z}_3$ symmetry. These symmetries can be summarized as follows:

$$\text{N2HDM and 2HDMS} \quad \mathbb{Z}_2: \Phi_1 \to \Phi_1, \qquad \Phi_2 \to -\Phi_2, \qquad S \to S \tag{2}$$

$$\text{N2HDM} \quad \mathbb{Z}_2': \Phi_1 \to \Phi_1, \qquad \Phi_2 \to \Phi_2, \qquad S \to -S \tag{3}$$

$$\text{2HDMS} \quad \mathbb{Z}_3: \begin{pmatrix} \Phi_1 \\ \Phi_2 \\ S \end{pmatrix} \to \begin{pmatrix} 1 & & \\ & e^{i2\pi/3} & \\ & & e^{-i2\pi/3} \end{pmatrix} \begin{pmatrix} \Phi_1 \\ \Phi_2 \\ S \end{pmatrix}. \tag{4}$$

The most general potential of two doublets and one singlet, before applying the $\mathbb{Z}_2$ or the additional $\mathbb{Z}_2'$ or the $\mathbb{Z}_3$ symmetry, is given by [45]

$$V = m_{11}^2 \Phi_1^\dagger \Phi_1 + m_{22}^2 \Phi_2^\dagger \Phi_2 - (m_{12}^2 \Phi_1^\dagger \Phi_2 + \text{h.c.})$$

$$+ \frac{\lambda_1}{2}(\Phi_1^\dagger \Phi_1)^2 + \frac{\lambda_2}{2}(\Phi_2^\dagger \Phi_2)^2 + \lambda_3(\Phi_1^\dagger \Phi_1)(\Phi_2^\dagger \Phi_2) + \lambda_4(\Phi_1^\dagger \Phi_2)(\Phi_2^\dagger \Phi_1)$$

$$+ \left[\frac{\lambda_5}{2}(\Phi_1^\dagger \Phi_2)^2 + \lambda_6(\Phi_1^\dagger \Phi_1)(\Phi_1^\dagger \Phi_2) + \lambda_7(\Phi_2^\dagger \Phi_2)(\Phi_1^\dagger \Phi_2) + \text{h.c.} \right]$$

$$+ (\xi S + \text{h.c.}) + m_S^2 S^\dagger S + \left(\frac{m_S'^2}{2} S^2 + \text{h.c.} \right)$$

$$+ \left(\frac{\mu_{S1}}{6} S^3 + \frac{\mu_{S2}}{2} S S^\dagger S + \text{h.c.} \right) + \left(\frac{\lambda_1''}{24} S^4 + \frac{\lambda_2''}{6} S^2 S^\dagger S + \text{h.c.} \right) + \frac{\lambda_3''}{4}(S^\dagger S)^2$$

$$+ [S(\mu_{11} \Phi_1^\dagger \Phi_1 + \mu_{22} \Phi_2^\dagger \Phi_2 + \mu_{12} \Phi_1^\dagger \Phi_2 + \mu_{21} \Phi_2^\dagger \Phi_1) + \text{h.c.}]$$

$$+ S^\dagger S[\lambda_1' \Phi_1^\dagger \Phi_1 + \lambda_2' \Phi_2^\dagger \Phi_2 + \lambda_3' \Phi_1^\dagger \Phi_2 + \text{h.c.}]$$

$$+ [S^2(\lambda_4' \Phi_1^\dagger \Phi_1 + \lambda_5' \Phi_2^\dagger \Phi_2 + \lambda_6' \Phi_1^\dagger \Phi_2 + \lambda_7' \Phi_2^\dagger \Phi_1) + \text{h.c.}] \tag{5}$$

with 29 free parameters.

For the N2HDM by applying the $\mathbb{Z}_2$ symmetry one finds that the parameters $\lambda_6, \lambda_7, \lambda_3', \lambda_6', \lambda_7'$, which break the $\mathbb{Z}_2$ symmetry explicitly, are zero. Applying the $\mathbb{Z}_2$ symmetry requires all linear or cubic terms in Φ_1 or Φ_2 to be zero. On the other hand, we keep m_{12}, which softly breaks the $\mathbb{Z}_2$ symmetry. Furthermore, since the S is real, one has $S^\dagger = S$. Applying the $\mathbb{Z}_2'$ symmetry eliminates all terms linear or odd in S. Summing up all terms containing $S^2 \Phi_1 \Phi_1, S^2 \Phi_2 \Phi_2, S^4$ allows to redefine accordingly the coefficients $\lambda_1' + \lambda_4', \lambda_2' + \lambda_5'$ and $\lambda_1'' + \lambda_2''$ as $\lambda_7, \lambda_8, \lambda_6$ respectively (to meet the definitions in [42]). The potential then reads

$$V_{\text{N2HDM}} = m_{11}^2 \Phi_1^\dagger \Phi_1 + m_{22}^2 \Phi_2^\dagger \Phi_2 - (m_{12}^2 \Phi_1^\dagger \Phi_2 + \text{h.c.}) + \frac{\lambda_1}{2}(\Phi_1^\dagger \Phi_1)^2 + \frac{\lambda_2}{2}(\Phi_2^\dagger \Phi_2)^2$$

$$+ \lambda_3(\Phi_1^\dagger \Phi_1)(\Phi_2^\dagger \Phi_2) + \lambda_4(\Phi_1^\dagger \Phi_2)(\Phi_2^\dagger \Phi_1) + \frac{\lambda_5}{2}[(\Phi_1^\dagger \Phi_2)^2 + \text{h.c.}]$$

$$+ \frac{1}{2} m_S^2 S^2 + \frac{\lambda_6}{8} S^4 + \frac{\lambda_7}{2}(\Phi_1^\dagger \Phi_1)S^2 + \frac{\lambda_8}{2}(\Phi_2^\dagger \Phi_2)S^2. \tag{6}$$

For the 2HDMS the effects of the $\mathbb{Z}_2$ symmetry are as for the N2HDM. Furthermore, by imposing the $\mathbb{Z}_3$ symmetry, we set the $\mathbb{Z}_3$-breaking parameters $\lambda_5 = \lambda_1'' = \lambda_2'' = \lambda_4' = \lambda_5' = 0$. On the other hand, we keep the terms

$m'_S, m_{12}, \mu_{S2}, \mu_{11}, \mu_{22}, \mu_{21}$, which softly break the $\mathbb{Z}_3$ symmetry. Taking the mapping of the 2HDMS to the NMSSM in [45] into account, we only keep m_{12} and μ_{12} as soft breaking parameters. The $\mathbb{Z}_3$-invariant scalar potential of the 2HDMS is given by

$$
\begin{aligned}
V_{\text{2HDMS}} = {}& m_{11}^2(\Phi_1^\dagger\Phi_1) + m_{22}^2(\Phi_2^\dagger\Phi_2) + \frac{\lambda_1}{2}(\Phi_1^\dagger\Phi_1)^2 + \frac{\lambda_2}{2}(\Phi_2^\dagger\Phi_2)^2 + \lambda_3(\Phi_1^\dagger\Phi_1)(\Phi_2^\dagger\Phi_2) \\
&+ \lambda_4(\Phi_1^\dagger\Phi_2)(\Phi_2^\dagger\Phi_1) + m_S^2(S^\dagger S) + \lambda_1'(S^\dagger S)(\Phi_1^\dagger\Phi_1) + \lambda_2'(S^\dagger S)(\Phi_2^\dagger\Phi_2) \\
&+ \frac{\lambda_3''}{4}(S^\dagger S)^2 + \left(-m_{12}^2\Phi_1^\dagger\Phi_2 + \frac{\mu_{S1}}{6}S^3 + \mu_{12}S\Phi_1^\dagger\Phi_2 + \text{h.c.} \right).
\end{aligned}
\tag{7}
$$

In this potential, the parameters λ_3'', λ_1', and λ_2' play the similar roles of λ_6, λ_7, λ_8, respectively in the N2HDM Higgs potential shown in Eq. (6), while the λ_5 term is forbidden by the $\mathbb{Z}_3$ symmetry in the 2HDMS. In addition, we have the new terms μ_{12} and μ_{S1} compared to the N2HDM, which arise from the complex singlet.

One can define $\tan\beta := v_2/v_1$ as in the 2HDM. Therefore, we obtain the $v = \sqrt{v_1^2 + v_2^2} \approx 174$ GeV based on our convention of the doublet fields (internally for the N2HDM we use a definition with an additional factor of $1/\sqrt{2}$). By using the minimization conditions

$$
\left.\frac{\partial V}{\partial \Phi_1}\right|_{\substack{\Phi_1=v_1 \\ \Phi_2=v_2 \\ S=v_S}} = \left.\frac{\partial V}{\partial \Phi_2}\right|_{\substack{\Phi_1=v_1 \\ \Phi_2=v_2 \\ S=v_S}} = \left.\frac{\partial V}{\partial S}\right|_{\substack{\Phi_1=v_1 \\ \Phi_2=v_2 \\ S=v_S}} = 0
\tag{8}
$$

m_{11}^2, m_{22}^2, and m_S^2 can be replaced by the expression from the tadpole equations. In the 2HDMS we now have 12 free parameters,

$$
\tan\beta, \ \lambda_1, \ \lambda_2, \ \lambda_3, \ \lambda_4, \ \lambda_1', \ \lambda_2', \ \lambda_3'', \ m_{12}^2, \ \mu_{S1}, \ \mu_{12}, \ v_S.
\tag{9}
$$

Similarly we have 11 free parameters in the N2HDM,

$$
\tan\beta, \ \lambda_1, \ \lambda_2, \ \lambda_3, \ \lambda_4, \ \lambda_5, \ \lambda_6, \ \lambda_7, \ \lambda_8 \ m_{12}^2, \ v_S.
\tag{10}
$$

These two different sets of input parameters lead to differences in the mass and mixing angle input and is discussed in Appendix A.

B. Masses and couplings

Due to the configuration of the fields, the charged Higgs sector of the N2HDM and 2HDMS have the same structure as the 2HDM. However, the additional singlet enters the neutral Higgs sector and mixes with two doublets for both *CP*-even sector and *CP*-odd sector. This generates an additional scalar Higgs in both models and in the case of the 2HDMS also an additional pseudoscalar Higgs. In total we have three scalar Higgs bosons h_1, h_2, h_3, the charged Higgs boson $H^\pm$, as well as two pseudoscalar

Higgs bosons a_1, a_2 for the 2HDMS, or one pseudoscalar Higgs boson a_1 for the N2HDM. We apply the conventions of $m_{h_1} < m_{h_2} < m_{h_3}$ and $m_{a_1} < m_{a_2}$ for the remainder of the paper.

We obtain the *CP*-even Higgs-boson mass eigenstates by diagonalizing the 3×3 mass matrix, M_S^2. Since this matrix is symmetric, the diagonalization matrix is orthogonal, given by the same 3×3 rotation matrix for the 2HDMS and N2HDM. For the *CP*-even sector, the rotation matrix reads

$$
R = \begin{pmatrix}
c_{\alpha_1} c_{\alpha_2} & s_{\alpha_1} c_{\alpha_2} & s_{\alpha_2} \\
-s_{\alpha_1} c_{\alpha_3} - c_{\alpha_1} s_{\alpha_2} s_{\alpha_3} & c_{\alpha_1} c_{\alpha_3} - s_{\alpha_1} s_{\alpha_2} s_{\alpha_3} & c_{\alpha_2} s_{\alpha_3} \\
s_{\alpha_1} s_{\alpha_3} - c_{\alpha_1} s_{\alpha_2} c_{\alpha_3} & -s_{\alpha_1} s_{\alpha_2} c_{\alpha_3} - c_{\alpha_1} s_{\alpha_3} & c_{\alpha_2} c_{\alpha_3}
\end{pmatrix},
\tag{11}
$$

where α_1, α_2, and α_3 are the three mixing angles. The mass basis and the interaction basis are related by

$$
\begin{pmatrix} h_1 \\ h_2 \\ h_3 \end{pmatrix} = R \begin{pmatrix} \rho_1 \\ \rho_2 \\ \rho_S \end{pmatrix}, \qquad \text{diag}\{m_{h_1}^2, m_{h_2}^2, m_{h_3}^2\} = R^T M_S^2 R.
\tag{12}
$$

In the *CP*-odd sector, taking into account the neutral Goldstone boson, in the 2HDMS we need two mixing angles for the diagonalization. The first one is, as in the 2HDM, the angle β. Additionally we define the angle α_4 for pseudoscalar Higgs bosons, and the mixing matrix for *CP*-odd sector can be expressed as

$$
R^A = \begin{pmatrix}
-s_\beta c_{\alpha_4} & c_\beta c_{\alpha_4} & s_{\alpha_4} \\
s_\beta s_{\alpha_4} & -c_\beta s_{\alpha_4} & c_{\alpha_4} \\
c_\beta & s_\beta & 0
\end{pmatrix}
\tag{13}
$$

$$
\text{with} \quad \begin{pmatrix} a_1 \\ a_2 \\ \xi \end{pmatrix} = R^A \begin{pmatrix} \eta_1 \\ \eta_2 \\ \eta_S \end{pmatrix},
$$

$$
\text{diag}\{m_{a_1}^2, m_{a_2}^2, 0\} = (R^A)^T M_P^2 R^A,
\tag{14}
$$

where the ξ denotes the Goldstone boson. In the N2HDM this reduces to a 2×2 rotation matrix (as in the 2HDM),

$$R^A = \begin{pmatrix} c_\beta & s_\beta \\ -s_\beta & c_\beta, \end{pmatrix}. \qquad (15)$$

By using the rotation matrices, one can express the free parameters of the Lagrangian in Eqs. (9) and (10) in terms of the masses of all Higgs bosons and the mixing angles (see Appendix A for details). As a result we have new sets of input parameters. For the 2HDMS we have

$$\tan\beta, \quad \alpha_{1,2,3,4}, \quad m_{h_1}, \quad m_{h_2}, \quad m_{h_3}, \quad m_{a_1}, \quad m_{a_2}, \quad m_{H^\pm}, \quad v_S \qquad (16)$$

and

$$\tan\beta, \quad \alpha_{1,2,3}, \quad m_{h_1}, \quad m_{h_2}, \quad m_{h_3}, \quad m_{a_1}, \quad m_{12}^2, \quad m_{H^\pm}, \quad v_S \qquad (17)$$

for the N2HDM. Naturally, the parameters α_4 and m_{a_2} are absent in the N2HDM. However, the different symmetry structure with respect to the 2HDMS leaves m_{12}^2 as additional free parameter. The corresponding situation in the 2HDMS is slightly more involved. When the singlet field acquires the vev, $\mu_{12} S \Phi_1^\dagger \Phi_2$ yields a term $v_S \mu_{12} \Phi_1^\dagger \Phi_2$, which is similar to the term $m_{12}^2 \Phi_1^\dagger \Phi_2$ in the N2HDM. In the 2HDMS mass basis, see Eq. (16), there is no free input parameter as m_{12}^2 due to the $\mathbb{Z}_3$ symmetry. However, the term $\sim \Phi_1^\dagger \Phi_2$ is generated by v_S, the CP-odd Higgs masses and mixing angle, i.e. μ_{12} can be converted to a combination of m_{a_1}, m_{a_2} and α_4.

For our analysis we interpret the experimental excess at ~ 96 GeV as the lightest scalar Higgs boson h_1, and we identify the second lightest scalar Higgs h_2 as the SM-like Higgs at ~ 125 GeV.

Furthermore, the elements of the rotation matrix, i.e. $|R_{ij}|^2$, represent each field admixtures of the corresponding physical states. The matrix elements thus determine the Higgs-boson couplings to the SM particles. Here we define the reduced coupling as the ratio between the 2HDMS/N2HDM Higgs coupling and the corresponding SM-Higgs coupling:

$$c_{h_i ff} = \frac{g_{h_i ff}}{g_{H_{\mathrm{SM}} ff}}. \qquad (18)$$

The reduced Higgs to fermion couplings for all four Yukawa types are summarized in Table I.

One can also derive the reduced Higgs to gauge-bosons couplings,

$$c_{h_i VV} = c_{h_i ZZ} = c_{h_i WW} = \cos\beta R_{i1} + \sin\beta R_{i2}. \qquad (19)$$

TABLE I. Higgs to fermion reduced couplings for different types of Yukawa couplings.

	Type I	Type II	Lepton specific	Flipped
$c_{h_i tt}$	$\frac{R_{i2}}{\sin\beta}$	$\frac{R_{i2}}{\sin\beta}$	$\frac{R_{i2}}{\sin\beta}$	$\frac{R_{i2}}{\sin\beta}$
$c_{h_i bb}$	$\frac{R_{i2}}{\sin\beta}$	$\frac{R_{i1}}{\cos\beta}$	$\frac{R_{i2}}{\sin\beta}$	$\frac{R_{i1}}{\cos\beta}$
$c_{h_i \tau\tau}$	$\frac{R_{i2}}{\sin\beta}$	$\frac{R_{i1}}{\cos\beta}$	$\frac{R_{i1}}{\cos\beta}$	$\frac{R_{i2}}{\sin\beta}$

C. Type II SM-like Higgs boson

Following Eq. (11), one finds that the singlet component of h_1 can be expressed by $|R_{13}|^2 = \sin^2 \alpha_2$. In our study, the lightest scalar Higgs h_1 should be a singlet-dominant Higgs, which is motivated by the experimental excesses, see the discussion below, i.e. $\sin^2 \alpha_2$ should be close to 1.

Since the type II N2HDM is favored for interpreting the experimental excess [21–25], we will stick to the type II Yukawa structure for our analysis. We choose h_2 to be the SM-like Higgs, and one can obtain the reduced couplings of h_2 to t-quark, b-quark and gauge bosons from Table I, Eq. (11) and Eq. (19),

$$c_{h_2 tt} = (c_{\alpha_1} c_{\alpha_3} - s_{\alpha_1} s_{\alpha_2} s_{\alpha_3})/s_\beta, \qquad (20)$$

$$c_{h_2 bb} = (-s_{\alpha_1} c_{\alpha_3} - c_{\alpha_1} s_{\alpha_2} s_{\alpha_3})/c_\beta, \qquad (21)$$

$$c_{h_2 VV} = c_{\alpha_3} s_{\beta-\alpha_1} - s_{\alpha_2} s_{\alpha_3} c_{\beta-\alpha_1}. \qquad (22)$$

In the limit of $\sin^2 \alpha_2 \to 1$, one can factor out $|\sin\alpha_2|$, and the h_2 couplings are approximately given by

$$c_{h_2 tt} \approx \frac{\cos(\alpha_1 + \mathrm{sgn}(\alpha_2)\alpha_3)}{\sin\beta} |\sin\alpha_2|, \qquad (23)$$

$$c_{h_2 bb} \approx -\frac{\sin(\alpha_1 + \mathrm{sgn}(\alpha_2)\alpha_3)}{\cos\beta} |\sin\alpha_2|, \qquad (24)$$

$$c_{h_2 VV} \approx \sin(\beta - (\alpha_1 + \mathrm{sgn}(\alpha_2)\alpha_3)) |\sin\alpha_2|. \qquad (25)$$

These three reduced couplings, Eqs. (23)–(25), are required to be close to 1 for an SM-like h_2. The so-called alignment limit is thus reached for $\beta - (\alpha_1 + \mathrm{sgn}(\alpha_2)\alpha_3) \to \pi/2$. All three couplings of the h_2 are close to 1 simultaneously in this limit.

D. Differences between the 2HDMS and the N2HDM

As discussed above, the 2HDMS has an additional CP-odd Higgs boson and additional mixing angle α_4 compared to the N2HDM, because of the imaginary part of the singlet field. Therefore, the α_4 determines whether the lighter a_1 or the heavier a_2 plays the role of the singletlike CP-odd Higgs. By taking our convention for the CP-odd mixing matrix in Eq. (13), the lighter CP-odd Higgs a_1 would be singlet dominated when $\alpha_4 \to \pi/2$. Conversely, when

$\alpha_4 \to 0$, the a_1 would be doubletlike and the heavier a_2 becomes singletlike. If $\alpha_4 = \pi/4$, both a_1 and a_2 are the admixture of the singlet component and the doublet components. In the case $\alpha_4 \to \pi/4$, one could potentially distinguish the *CP*-odd Higgs A in N2HDM from the *CP*-odd Higgs a_i in 2HDMS with singlet admixture, by comparing the decays of $A/a_i \to \tau^+\tau^-$ or $A/a_i \to t\bar{t}$. On the other hand, if α_4 is too close to 0 or $\pi/2$, the singlet dominant *CP*-odd Higgs would completely decouple from the other SM particles, where the 2HDMS can be approximately in the "N2HDM limit," and only the doubletlike *CP*-odd Higgs of the 2HDMS would remain potentially visible. In this case it would be difficult to resolve experimentally the difference in the couplings of the doubletlike *CP*-odd Higgs to fermions.

However, even in the limit of $\alpha_4 = 0$ or $\pi/2$ the two models differ by their symmetries. The $\mathbb{Z}_3$ symmetry of the 2HDMS yields two additional trilinear terms μ_{12} and μ_{S1} in the Higgs potential. By neglecting the effect of the imaginary part of the singlet field, the λ_1', λ_2' and λ_3'' in Eq. (7) can play the similar roles of λ_7, λ_8 and λ_6 in Eq. (6), respectively. On the other hand, the terms given by μ_{S1} and μ_{12} have no corresponding terms in the N2HDM. Consequently, these two terms can give an additional contribution on the triple-Higgs couplings which can be expressed as

$$\lambda_{h_i h_j h_k} = \lambda_{h_i h_j h_k}^{\text{N2HDM-like}} + \frac{\mu_{S1}}{2v} R_{i3} R_{j3} R_{k3}$$
$$+ \frac{\mu_{12}}{2v} [(R_{i2} R_{j3} + R_{j2} R_{i3}) R_{k1}$$
$$+ (R_{i1} R_{j3} + R_{j1} R_{i3}) R_{k2} + (R_{i1} R_{j2} + R_{j2} R_{i1}) R_{k3}].$$

(26)

Here the N2HDM-like part is the N2HDM triple Higgs couplings, but replacing the $\lambda_7, \lambda_8, \lambda_6$ by the $\lambda_1', \lambda_2', \lambda_3''$. In the limit of $\alpha_4 = 0$ or $\pi/2$, one finds $\mu_{12} = 0$ according to Eq. (A6). However, μ_{S1} would be nonzero as long as the singlet *CP*-odd Higgs remains massive. In this case, the additional μ_{S1} contributions can lead to differences in $\lambda_{h_1 h_1 h_1}$, $\lambda_{h_1 h_1 h_2}$ and $\lambda_{h_1 h_2 h_2}$, since μ_{S1} is the trilinear self-coupling of the singlet field and the h_1 is the singlet dominated Higgs. This would lead to differences, e.g., in various di-Higgs production modes at pp or e^+e^- colliders. On the other hand, the differences in the triple-Higgs couplings with h_3 involved would be relatively small and difficult to detect in the decay $h_3 \to h_i h_j$. We leave such studies for future work.

In principle, the μ_{S1} term can also vanish in the case of a massless *CP*-odd singlet Higgs according to (A8). In this case the triple-Higgs couplings can be similar in both models in the limit of $\alpha_4 \to \pi/2$ and $m_{a_1} \to 0$. However, the decay channel of $h_2 \to a_1 a_1$ would then be open ($m_{h_2} > 2m_{a_1}$), which would drastically change the behavior of the Higgs at ~ 125 GeV.

III. THE CONSTRAINTS

In this section we describe in detail the theoretical and experimental constraints applied in our analysis to the 2HDMS and N2HDM.

A. Theoretical constraints

The 2HDMS and N2HDM face constraints from tree-level perturbative unitarity, the condition that the potential should be bounded from below and the stability of the vacuum. In the following we show the conditions for the 2HDMS. All constraints for the N2HDM were already derived in [42] (see below).

(i) Tree-level perturbative unitarity

Tree-level perturbative unitarity conditions ensure perturbativity of the model up to very high scales. This can be achieved by demanding the amplitudes of the scalar quartic interactions, which are given by the eigenvalues of the $2 \to 2$ scattering matrix, to be below a value of 8π. The calculation was carried out with a *Mathematica* package implemented in SCANNERS [46] and by following the procedure of [47]. The conditions are

$$|\lambda_{1,2}'| < 8\pi \tag{27}$$

$$\left| \frac{\lambda_3''}{2} \right| < 8\pi \tag{28}$$

$$|\lambda_{1,2,3}| < 8\pi \tag{29}$$

$$|\lambda_3 \pm \lambda_4| < 8\pi \tag{30}$$

$$\left| \frac{1}{2} \left(\lambda_1 + \lambda_2 \pm \sqrt{(\lambda_1 - \lambda_2)^2 + 4\lambda_4^2} \right) \right| < 8\pi \tag{31}$$

For models with extended scalar sectors the calculation cannot be carried out purely analytically. The remaining eigenvalues are given by the three real roots (x_1, x_2, x_3) of the cubic polynomial

$$64(6\lambda_2'^2 \lambda_1 + 6\lambda_1'^2 \lambda_2 - 9\lambda_3'' \lambda_1 \lambda_2 - 8\lambda_1' \lambda_2' \lambda_3 + 4\lambda_3'' \lambda_3^2$$
$$- 4\lambda_1' \lambda_2' \lambda_4 + 4\lambda_3'' \lambda_3 \lambda_4 + \lambda_3'' \lambda_4^2)$$
$$+ 16(-2\lambda_1'^2 - 2\lambda_2'^2 + 3\lambda_3'' \lambda_1 + 3\lambda_3'' \lambda_2 + 9\lambda_1 \lambda_2$$
$$- 4\lambda_3^2 - 4\lambda_3 \lambda_4 - \lambda_4^2)x$$
$$+ (-4\lambda_3'' - 12\lambda_1 - 12\lambda_2)x^2 + x^3 = 0 \tag{32}$$

$$\left| \frac{x_1}{4} \right| < 8\pi, \qquad \left| \frac{x_2}{4} \right| < 8\pi, \qquad \left| \frac{x_3}{4} \right| < 8\pi. \tag{33}$$

The corresponding conditions for the N2HDM were already derived in [42] [see their Eqs. (3.43)–(3.48)].

(ii) Boundedness from below

The boundedness from below conditions ensure that the potential remains positive when the field values approach infinity. The conditions can be found in [48] and were adapted for the 2HDMS. The allowed region is given by

$$\Omega_1 \cup \Omega_2 \tag{34}$$

with

$$\Omega_1 = \left\{ \lambda_1, \lambda_2, \lambda_3'' > 0; \sqrt{\frac{\lambda_1 \lambda_3''}{2}} + \lambda_1' > 0; \sqrt{\frac{\lambda_2 \lambda_3''}{2}} + \lambda_2' > 0; \right. \tag{35}$$

$$\left. \sqrt{\lambda_1 \lambda_2} + \lambda_3 + D > 0; \lambda_1' + \sqrt{\frac{\lambda_1}{\lambda_2}} \lambda_2' \geq 0 \right\} \tag{36}$$

and

$$\Omega_2 = \left\{ \lambda_1, \lambda_2, \lambda_3'' > 0; \sqrt{\frac{\lambda_2 \lambda_3''}{2}} \geq \lambda_2' > -\sqrt{\frac{\lambda_2 \lambda_3''}{2}}; -\sqrt{\frac{\lambda_1}{\lambda_2}} \lambda_2' \geq \lambda_1' > -\sqrt{\frac{\lambda_1 \lambda_3''}{2}}; \right. \tag{37}$$

$$\left. \frac{(D + \lambda_3)\lambda_3''}{2} > \lambda_1' \lambda_2' - \sqrt{\left(\lambda_1'^2 - \frac{\lambda_1 \lambda_3''}{2} \right) \left(\lambda_2'^2 - \frac{\lambda_2 \lambda_3''}{2} \right)} \right\}, \tag{38}$$

where

$$D = \begin{cases} \lambda_4 & \text{for } \lambda_4 < 0 \\ 0 & \text{for } \lambda_4 \geq 0. \end{cases} \tag{39}$$

The corresponding conditions for the N2HDM were already derived in [42] [see their Eqs. (3.51) and (3.52)].

(iii) Vacuum stability

In the SM the electroweak (EW) vacuum is required to be stable at the EW scale. This vacuum state is characterized by a nonzero vev of the Higgs field. In BSM theories vacuum stability at the EW scale places additional constraints on their extended parameter space. An obvious condition is to require the EW vacuum to be the global minimum (*true vacuum*) of the scalar potential. In this case the EW is absolutely stable. If the EW vacuum is a local minimum (*false vacuum*) the corresponding parameter region can still be allowed if it is sufficiently metastable. This is the case if the predicted lifetime of the false vacuum is longer than the current age of the universe. Any configuration with a lifetime shorter than the age of the universe is considered unstable.

For our study we used EVADE [49–51] which finds the tree-level minima employing HOM4PS2 [52]. In the case of the EW vacuum being a false vacuum, it calculates the bounce action for a given parameter point with a straight path approximation, which is sufficiently accurate for the purpose, see [50]. Points with a bounce action $B > 440$ are considered to be long-lived. We compared the results of the straight path approximation of EVADE with the more sophisticated approach via path deformation of the code FINDBOUNCE [53]. We found the enhancement by the computationally more intensive FINDBOUNCE to be negligible. Additionally we compared the results of EVADE with the code VEVACIOUS++ [54,55]. The latter incorporates the tree level as well as the Coleman-Weinberg one-loop potential. While the one-loop effective potential approach of VEVACIOUS++ [55]. suffers from numerical instabilities, the tree-level results placed a stricter constraint on the long-lived regions, but were in good agreement with EVADE. We therefore chose the actively developed code EVADE (which is based on VEVACIOUS).

B. Experimental constraints

The set of experimental constraints from searches at colliders are the same for both the 2HDMS and the N2HDM.

(i) Higgs-boson rate measurements

We use the public code HIGGSSIGNALS-2.6.1 [56–61] to verify that all generated points agree with currently available measurements of the SM Higgs-boson. HIGGSSIGNALS calculates the χ^2_{HS} from

the comparison of the model prediction with the Higgs-boson signal rates and masses at Tevatron and LHC. The complete list of implemented constraints can be found in [56]. In our analysis we use the reduced χ^2 to judge the validity of our generated points, which is defined as

$$\chi^2_{\text{red}} = \frac{\chi^2_{\text{HS}}}{n_{\text{obs}}}. \tag{40}$$

Here χ^2 is evaluated by HIGGSSIGNALS and $n_{\text{obs}} = 111$ is the considered number of experimental measurements.

(ii) BSM Higgs-boson searches

The public code HIGGSBOUNDS-5.9.1 [58–61] provides 95% confidence level exclusion limits of all relevant direct searches for charged Higgs bosons and additional neutral Higgs bosons. Searches for charged Higgs bosons put constraints on the allowed $M_{H^\pm} - \tan\beta$ regions in the 2HDM [62]. Since the charged sector is identical in the 2HDMS the constraints on the parameter space can be directly taken over. Important searches are the direct searches for charged Higgs production $pp \to H^\pm tb$ with the decay modes $H^\pm \to \tau\nu$ and $H^\pm \to tb$ [63]. The constrained regions mostly lie in the low $\tan\beta \lesssim 2$ region, due to the enhanced coupling to top quarks. Searches at LEP for charged Higgs bosons are mostly irrelevant as we focus on $\tan\beta = \{1, 20\}$ and light charged Higgs-boson masses are excluded from flavor physics observables (see below).

Direct searches for additional neutral Higgs-bosons are relevant when the heavy scalar Higgs-boson h_3 or the heavy pseudoscalar Higgs bosons a_1, a_2 are not too heavy.

(iii) Flavor physics observables

The presence of additional Higgs Bosons in 2HDM-type models leads to constraints from flavor physics. The charged Higgs sector of the 2HDMS or N2HDM is unaltered with respect to the general 2HDM. For the $\tan\beta = \{1, 20\}$ region we are interested in, the most important bounds according to [62] come from the branching ratio $\text{BR}(B_s \to X_s\gamma)$, constraints on ΔM_{B_s} come from the branching ratio $\text{BR}(B_s \to \mu^+\mu^-)$. The dominant contributions to these bounds come from charged Higgs $H^\pm$ [64–66] and top quarks [67,68]. As they are independent from the neutral scalar sector to a good approximation we can take over the bounds directly from the 2HDM. The constraints from ΔM_{B_s} and $\text{BR}(B_s \to \mu^+\mu^-)$ are dominant for $\tan\beta \simeq 1$ while the constraint from $\text{BR}(B_s \to X_s\gamma)$ is present for the whole range of $\tan\beta$ we study. Taking all this into account for our study in the

type II 2HDMS and N2HDM, these constraints give a lower limit of the charged Higgs mass of $m_{H^\pm} \gtrsim 650$ GeV [62].

(iv) Electroweak precision observables

If BSM physics enters mainly through gauge boson self-energies, as it is the case for the extended Higgs sector of the 2HDMS and the N2HDM, constraints from electroweak precision observables can be expressed in terms of the parameters S, T, and U [69], revealing significant changes from BSM to these parameters. SPHENO has implemented the one-loop corrections of these parameters for any model with additional doublets and singlets. If the gauge group is the SM $SU(2) \times U(1)$ and BSM particles have suppressed couplings to light SM fermions, the corrections are independent of the Yukawa type of the model. The differences of the masses of the scalars have a large impact on these corrections. They are small if the heavy Higgs mass h_3 or the heavy doubletlike pseudoscalar mass are close to the charged Higgs-boson mass [69]. In the 2HDMS and the N2HDM the parameter T is most sensitive and has a strong correlation to U. Contributions to U can therefore be dropped [22]. For our scan we require the prediction of the S and T parameters to be within the 95% confidence level (CL) region, corresponding to $\chi^2 = 5.99$ for two degrees of freedom.

IV. THE PARAMETER SPACE EMBEDDING THE EXPERIMENTAL EXCESSES

In this section we first describe the theory predictions of the two models for the two excesses. We describe how we analyze the parameter spaces of the two models, emphasizing the differences. We then analyze first the parameter space in the 2HDMS which leads to a good description of the experimental excesses. Subsequently, we contrast this with the preferred parameter space in the N2HDM.

A. The 96 GeV "excesses"

The experimental excesses at both LEP and CMS could be translated to the following signal strengths as quoted in [11,14,70,71]:

$$\mu_{\text{LEP}}^{\text{exp}} = \frac{\sigma^{\text{exp}}(e^+e^- \to Z\phi \to Zb\bar{b})}{\sigma^{\text{SM}}(e^+e^- \to ZH_{\text{SM}}^0 \to Zb\bar{b})} = 0.117 \pm 0.05 \tag{41}$$

$$\mu_{\text{CMS}}^{\text{exp}} = \frac{\sigma^{\text{exp}}(pp \to \phi \to \gamma\gamma)}{\sigma^{\text{SM}}(pp \to H_{\text{SM}}^0 \to \gamma\gamma)} = 0.6 \pm 0.2, \tag{42}$$

where the H_{SM}^0 is the SM Higgs boson with the rescaled mass at the same range as the unknown scalar particle ϕ.

Since one of the most important targets of our analysis is the interpretation of the experimental excess in the 2HDMS/N2HDM, we interpreted the scalar ϕ as the

lightest CP-even Higgs boson h_1 of the 2HDMS/N2HDM, and we evaluated such signal strengths for all the h_1. These signal strengths can be calculated by the following expressions in the narrow width approximation [22] (introduced here for the 2HDMS):

$$
\begin{aligned}
\mu_{\mathrm{LEP}}^{\mathrm{the}} &= \frac{\sigma_{\mathrm{2HDMS}}(e^+e^- \to Zh_1)}{\sigma_{\mathrm{SM}}(e^+e^- \to ZH_{\mathrm{SM}}^0)} \times \frac{\mathrm{BR}_{\mathrm{2HDMS}}(h_1 \to b\bar{b})}{\mathrm{BR}_{\mathrm{SM}}(H_{\mathrm{SM}}^0 \to b\bar{b})} \\
&= |c_{h_1VV}|^2 \frac{\mathrm{BR}_{\mathrm{2HDMS}}(h_1 \to b\bar{b})}{\mathrm{BR}_{\mathrm{SM}}(H_{\mathrm{SM}}^0 \to b\bar{b})}
\end{aligned}
\tag{43}
$$

$$
\begin{aligned}
\mu_{\mathrm{CMS}}^{\mathrm{the}} &= \frac{\sigma_{\mathrm{2HDMS}}(gg \to h_1)}{\sigma_{\mathrm{SM}}(gg \to H_{\mathrm{SM}}^0)} \times \frac{\mathrm{BR}_{\mathrm{2HDMS}}(h_1 \to \gamma\gamma)}{\mathrm{BR}_{\mathrm{SM}}(H_{\mathrm{SM}}^0 \to \gamma\gamma)} \\
&= |c_{h_1tt}|^2 \frac{\mathrm{BR}_{\mathrm{2HDMS}}(h_1 \to \gamma\gamma)}{\mathrm{BR}_{\mathrm{SM}}(H_{\mathrm{SM}}^0 \to \gamma\gamma)}.
\end{aligned}
\tag{44}
$$

The effective couplings c_{h_1VV} and c_{h_1tt} can be easily obtained from Eq. (19) and Table I, while the corresponding branching ratios have been obtained with SPHENO-4.0.4 [72,73].

The overall χ^2 corresponding to the excesses is calculated as

$$
\chi_{\mathrm{CMS\text{-}LEP}}^2 = \left(\frac{\mu_{\mathrm{LEP}}^{\mathrm{the}} - 0.117}{0.057} \right)^2 + \left(\frac{\mu_{\mathrm{CMS}}^{\mathrm{the}} - 0.6}{0.2} \right)^2.
\tag{45}
$$

The total χ^2 is defined as

$$
\chi_{\mathrm{tot}}^2 = \chi_{\mathrm{CMS\text{-}LEP}}^2 + \chi_{\mathrm{HS}}^2.
\tag{46}
$$

The points of the 2HDMS/N2HDM with the lowest χ_{tot}^2 are the respective "best-fit" points in the two models.

In order to understand the effect of mixing angles on the signal strengths of the excesses, one can focus on the couplings of h_1 derived from Eq. (11) and Table I, which are given by

$$
c_{h_1tt} = \frac{\sin\alpha_1 \cos\alpha_2}{\sin\beta}, \qquad c_{h_1bb} = \frac{\cos\alpha_1 \cos\alpha_2}{\cos\beta},
$$
$$
c_{h_1VV} = \cos\alpha_2 \cos(\beta - \alpha_1).
\tag{47}
$$

If h_1 is the pure gauge singlet (i.e. $\cos\alpha_2 = 0$), all three couplings in Eq. (47), which are proportional to the $\cos\alpha_2$, would be zero. However, h_1 would then be completely invisible and could not produce any experimental excesses in this case. Therefore, in order to cover the ranges of the experimental excesses efficiently, we enforced the singlet component of h_1 to be smaller than 95% (i.e. $\cos^2\alpha_2 > 5\%$), which essentially yields nonvanishing couplings of h_1 to SM particles. As a result, the interval of α_2 is constrained by this requirement. We have checked explicitly that this constraint does not exclude any valid parameter point in our analysis.

For the signal strength of CMS, the coupling c_{h_1tt} and the BR($h_1 \to \gamma\gamma$) play the dominant roles. Since the decay width of the h_1 is dominated by the decay to $b\bar{b}$, a smaller c_{h_1bb} would suppress the decay width of $h_1 \to b\bar{b}$ and lead to the enhancement of BR($h_1 \to \gamma\gamma$). Consequently, BR($h_1 \to \gamma\gamma$) can be antiproportional to the coupling $|c_{h_1bb}|^2$. Since μ_{CMS} is also proportional to the $|c_{h_1tt}|^2$, one obtains the approximate relation for μ_{CMS} which is given by

$$
\mu_{\mathrm{CMS}}^{\mathrm{the}} \propto \frac{|c_{h_1tt}|^2}{|c_{h_1bb}|^2} = \left(\frac{\tan\alpha_1}{\tan\beta} \right)^2.
\tag{48}
$$

As we see in Eq. (48), $\mu_{\mathrm{CMS}}^{\mathrm{the}}$ can be directly enhanced by the increment of α_1. In order to have a not too suppressed signal strength for the CMS excess, $\tan\alpha_1 > \tan\beta$ is required. However, the combination $\frac{\tan\alpha_1}{\tan\beta}$ can be arbitrarily large during the scan. Thus we scan the inverse of this combination in the range from 0 to 1, see the next subsection.

B. Parameter scan

Following the N2HDM interpretation of the excesses [22], we focus on the type-II Yukawa structure also for the 2HDMS. However, we will investigate a larger $\tan\beta$ region as it was done in Ref. [22].

In order to investigate the parameter space of the 2HDMS/N2HDM that gives rise to a description of the 96 GeV excesses, we performed an extensive scan of the parameter spaces by using the spectrum generator SPHENO-4.0.4 [72,73], where the model implementations are generated by the public code SARAH-4.14.3 [74]. During the scan, we fix the mass $m_{h_2} = 125.09$ GeV and enforce the mixing angles to be close to the alignment limit as explained in detail in Sec. II C. As discussed above, by employing HIGGSSIGNAL-2.6.1, we can ensure that the h_2 is in agreement with the LHC measurements. Concerning the exclusion bounds from flavor physics as we mentioned in Sec. III B, we simply apply the conservative limits given by $\tan\beta > 1$ and $m_{H^\pm} > 800$ GeV, which is above the experimental limit of 650 GeV [62].

Studying a higher region of $\tan\beta$ with different ranges for the heavy Higgs-boson masses from 1 to 20 (i.e. going beyond the region explored in Ref. [22]) raises the lower bound of the heavy Higgs boson masses m_{h_3} and m_{a_2}

TABLE II. Heavy Higgs-boson mass scan intervals for different $\tan\beta$ regions.

$\tan\beta$	$m_{h_3} \sim m_{a_2} \sim m_{H^\pm}$
1–10	{800, 1200} GeV
10–20	{1000, 1700} GeV

coming from the constraints on heavy Higgs bosons from searches for $H/A \to \tau^+\tau^-$ at the LHC[75]. We scan two intervals of $\tan\beta$ with different ranges for the heavy Higgs-boson masses, see Table II. Concerning unitarity constraints and the S, T, U parameters, the mass difference between the heavy Higgs states has to be small. Therefore $m_{H^\pm}$ is scanned in the interval given in Table II and the other two are scanned around this mass with a Gaussian distribution (with a width of 200 or 50 GeV for the low and high $\tan\beta$ region, respectively).

In the case of the 2HDMS we have an additional lighter CP-odd Higgs boson a_1, see Sec. II D. For $\alpha_4 < \frac{\pi}{4}$ the heavier a_2 would be singletlike. This scenario is more likely to be excluded by vacuum stability constraints and we leave this for future studies. Therefore we choose $\frac{\pi}{4} < \alpha_4 < \frac{\pi}{2}$, which makes the lighter a_1 singletlike. We choose $m_{h_2} < m_{a_1}$ which leads to a scan range of m_{a_1} from 200 to 500 GeV to also fulfill $m_{a_1} < m_{a_2}$. Overall, the scan intervals for all the particles are given by

FIG. 1.   The signal strengths of both excesses $\mu_{\rm CMS}$ and $\mu_{\rm LEP}$ for the 2HDMS scan points with $\tan\beta \in \{1, 10\}$. The red ellipse shows the 1σ region of the excesses with the red star as the best-fit point. The color code indicates the $\chi^2_{\rm red}$ and the lowest $\chi^2_{\rm red}$ in the 1σ ellipse is about 0.821.

$$m_{h_1} \in \{95, 98\}\text{GeV}, \qquad m_{h_2} = 125.09 \text{ GeV}, \qquad m_{a_1} \in \{200, 500\}\text{GeV},$$

$$|\sin(\beta - (\alpha_1 + \text{sgn}(\alpha_2)\alpha_3))| \in \{0.98, 1\}, \qquad \alpha_4 \in \left\{\frac{\pi}{4}, \frac{\pi}{2}\right\}, \qquad v_S \in \{100, 2000\}\text{GeV},$$

$$\frac{\tan\beta}{\tan\alpha_1} \in \{0, 1\}, \qquad \alpha_2 \in \pm\{0.95, 1.3\}. \tag{49}$$

We have checked explicitly that the constraints on $\sin(\beta - (\alpha_1 + \text{sgn}(\alpha_2)\alpha 3))$ and α_2 do not exclude any valid point of our parameter space.

C. Preferred 2HDMS parameter spaces

The results of the 2HDMS scan in the low $\tan\beta$ region are shown in Fig. 1 in the $\mu_{\rm CMS}$-$\mu_{\rm LEP}$ plane, where the color cod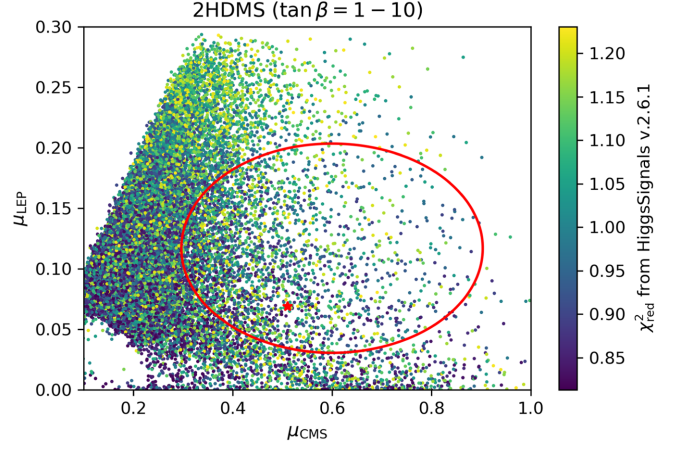e indicates $\chi^2_{\rm red}$, see Eq. (40). The red ellipse corresponds to the 1σ ellipse, with the best-fit point (see below) marked by a red cross.

As can be seen in Fig. 1 the 1σ ellipse of $\mu_{\rm CMS}$ and $\mu_{\rm LEP}$ can be fully covered by the 2HDMS parameter space, while all the points in the figure have $\chi^2_{\rm red} < 1.3$. The lowest $\chi^2_{\rm red}$ in the 1σ ellipse is about 0.821. Therefore, the 96 GeV

TABLE III.   Parameters and relevant branching ratios of the best-fit point in the 2HDMS in the $\tan\beta \in \{1, 10\}$ region.

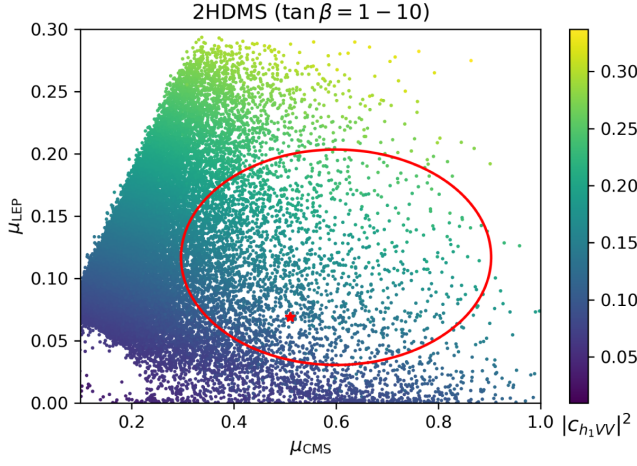| m_{h_1} 96.438 GeV	m_{h_2} 125.09 GeV	m_{h_3} 784.08 GeV	m_{a_1} 413.46 GeV	m_{a_2} 660.07 GeV	$m_{H^\pm}$ 808.93 GeV
$\tan\beta$	α_1	α_2	α_3	α_4	v_s
1.3393	1.3196	-1.1687	-1.2575	1.4719	653.84 GeV
		Branching ratios			
$h_1 \to b\bar{b}$	$h_1 \to gg$	$h_1 \to \tau^+\tau^-$	$h_1 \to \gamma\gamma$	$h_1 \to W^{+(*)}W^{-(*)}$	$h_1 \to Z^{(*)}Z^{(*)}$
42.2%	35.3%	4.61%	0.317%	0.739%	< 0.1%
$h_2 \to b\bar{b}$	$h_2 \to gg$	$h_2 \to \tau^+\tau^-$	$h_2 \to \gamma\gamma$	$h_2 \to W^{+(*)}W^{-(*)}$	$h_2 \to Z^{(*)}Z^{(*)}$
53.9%	10.5%	6.17%	0.249%	23.4%	2.54%
$h_3 \to b\bar{b}$	$h_3 \to t\bar{t}$	$h_3 \to h_2 h_2$	$h_3 \to h_1 h_2$	$h_3 \to h_1 h_1$	$h_3 \to W^+W^-$
< 0.1%	65.3%	5.26%	7.76%	0.158%	8.26%
$a_1 \to t\bar{t}$	$a_1 \to \tau^+\tau^-$	$a_2 \to t\bar{t}$	$a_2 \to \tau^+\tau^-$	$H^\pm \to tb$	$H^\pm \to W^\pm h_2$
95%	< 0.1%	88.2%	< 0.1%	73.7%	1.12%

FIG. 2. The same plane as in Fig. 1, with the color code indicating the square of the effective coupling of h_1 to gauge bosons. The lowest (highest) value of $|c_{h_1 VV}|^2$ in the 1σ ellipse is 0.088 (0.26).

excesses can be easily accommodated while the h_2 at ~125 GeV is in good agreement with the experimental measurements. The best-fit point, defined via Eq. (46), is marked with a red cross and lies well within the 1σ ellipse. Phenomenological details of this best-fit point can be found in Table III.

In Figs. 2 and 3 we show the results for $|c_{h_1 VV}|^2$ and $|c_{h_1 bb}/c_{h_1 tt}|^2$, respectively, in the plane of $\mu_{\rm CMS}$ and $\mu_{\rm LEP}$. In Fig. 2, the points with higher signal strength $\mu_{\rm LEP}$ always have the higher coupling $c_{h_1 VV}$, as $\mu_{\rm LEP}$ is directly proportional to $|c_{h_1 VV}|^2$, see Eq. (43). On the other hand, one can observe from Fig. 3 that the points with lower values of $|c_{h_1 bb}|^2/|c_{h_1 tt}|^2$ yield a higher signal strength $\mu_{\rm CMS}$,
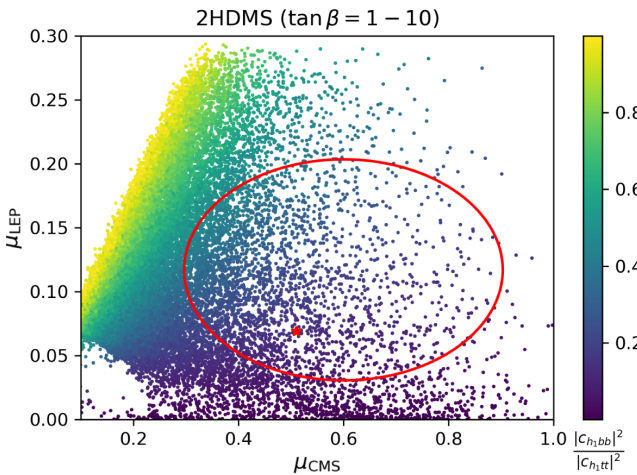
FIG. 3. The same plane as in Fig. 1, with the color code indicating the ratio $|c_{h_1 bb}|^2/|c_{h_1 tt}|^2$. The lowest (highest) value in the 1σ ellipse is 0.039 (0.53).
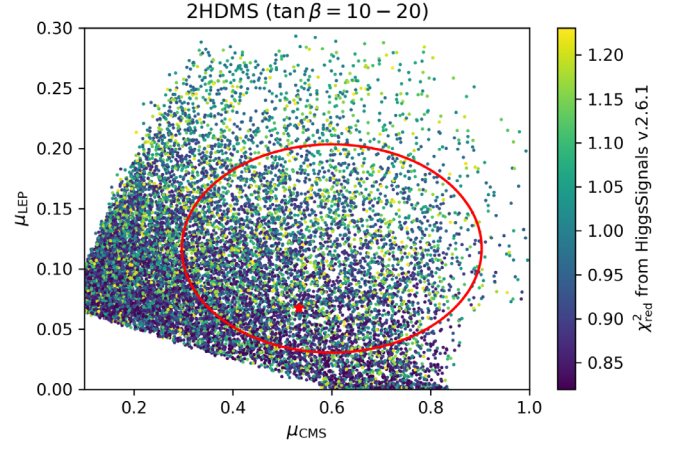

FIG. 4. The same plane as in Fig. 1 with $\tan\beta \in \{10, 20\}$, and the color coding indicating the $\chi^2_{\rm red}$.

consistent with the discussion in Sec. IV A, i.e. $\mu_{\rm CMS}$ is antiproportional to $|c_{h_1 bb}|^2/|c_{h_1 tt}|^2$. However, a lower $c_{h_1 bb}$ coupling would slightly suppress BR($h_1 \to b\bar{b}$) that lead to the lower $\mu_{\rm LEP}$, and therefore the distribution is slightly oblique in the plane of $\mu_{\rm CMS}$ and $\mu_{\rm LEP}$. The best-fit point marked by the red cross has $|c_{h_1 VV}|^2 \sim 0.13$ and $|c_{h_1 bb}|^2/|c_{h_1 tt}|^2 \sim 0.12$.

The results of the high $\tan\beta$ region scan, using the scan intervals given in Table II, are shown in Fig. 4, where the color coding indicates the $\chi^2_{\rm red}$. It can be observed that also in the high $\tan\beta$ region the 1σ ellipse in the plane of $\mu_{\rm CMS} - \mu_{\rm LEP}$ is well covered by our parameter scan for $\tan\beta = 10$–20. The distribution of the $\chi^2_{\rm red}$ is found to be very similar to the low $\tan\beta$ case. Also the other quantities, $|c_{h_1 VV}|^2$ and $|c_{h_1 bb}|^2/|c_{h_1 tt}|^2$, behave as in the low $\tan\beta$ case (and are thus not shown). In Table IV we summarize the details for best-fit points in the region of $\tan\beta = 10$–20. The high $\tan\beta$ best-fit point has $|c_{h_1 VV}|^2 \sim 0.12$ and $|c_{h_1 bb}/c_{h_1 tt}|^2 \sim 0.14$, which is very close to the corresponding numbers of the low $\tan\beta$ best-fit point. Overall we find that the points within the 1σ range of the 96 GeV excesses have no preference for low or high $\tan\beta$. Finally, also for the charged Higgs-boson mass we do not find a preferred region (within the intervals given in Table II), neither in the low nor in the high $\tan\beta$ analysis.

D. Preferred N2HDM parameter spaces

We now turn to the corresponding analysis in the N2HDM, where earlier results can be found in Refs. [21–25]. In Fig. 5 we show the results of the N2HDM in the $\mu_{\rm CMS}$-$\mu_{\rm LEP}$ plane for the low (left plot) and high $\tan\beta$ range (right plot). One can observe that both the low $\tan\beta$ region and the high $\tan\beta$ region of the

TABLE IV. Parameters and relevant branching ratios of the best-fit point in the high $\tan\beta$ region.

Best-fit point in $\tan\beta \in \{10, 20\}$					
m_{h_1} 96.013 GeV	m_{h_2} 125.09 GeV	m_{h_3} 1437.8 GeV	m_{a_1} 323.4 GeV	m_{a_2} 1438.5 GeV	$m_{H^\pm}$ 1499.6 GeV
$\tan\beta$	α_1	α_2	α_3	α_4	v_s
13.783	1.5441	1.2162	1.5338	1.5679	1212.6 GeV
Branching ratios					
$h_1 \to b\bar{b}$	$h_1 \to gg$	$h_1 \to \tau^+\tau^-$	$h_1 \to \gamma\gamma$	$h_1 \to W^{+(*)}W^{-(*)}$	$h_1 \to Z^{(*)}Z^{(*)}$
45.1%	32.5%	4.93%	0.612%	1.04%	$< 0.1\%$
$h_2 \to b\bar{b}$	$h_2 \to gg$	$h_2 \to \tau^+\tau^-$	$h_2 \to \gamma\gamma$	$h_2 \to W^{+(*)}W^{-(*)}$	$h_2 \to Z^{(*)}Z^{(*)}$
53.7%	10.0%	6.14%	0.269%	24.2%	2.62%
$h_3 \to b\bar{b}$	$h_3 \to t\bar{t}$	$h_3 \to h_2 h_2$	$h_3 \to h_1 h_2$	$h_3 \to h_1 h_1$	$h_3 \to W^+ W^-$
69.7%	4.82%	3.74%	5.73%	0.585%	2.60%
$a_1 \to b\bar{b}$	$a_1 \to \tau^+\tau^-$	$a_2 \to b\bar{b}$	$a_2 \to \tau^+\tau^-$	$H^\pm \to tb$	$H^\pm \to W^\pm h_2$
88.0%	11.7%	74.2%	12%	91.4%	0.353%

N2HDM parameter space can cover the 1σ range of the 96 GeV "excess". This extends the analysis in Ref. [22], where only relatively low $\tan\beta$ values were found. These differences can be traced back to an improved scan strategy as well as improvements in the parameter point generation. The behavior of the other quantities analyzed in the previous subsection is very similar for the N2HDM.

Overall, our comparative analysis of the 2HDMS (which is a new model analysis) and the N2HDM (updating the results of Ref. [22]) shows that the two models can fit equally well the 96 GeV excesses. The differences between the two models (see in particular the discussion in Sec. II, i.e. different symmetries and different particle content) do not impact in a relevant way the description of the excesses. Consequently, other phenomenological investigations will have to be performed to distinguish the two models, see the discussion in Sec. II D, but also our analysis below in Secs. V A and V B.

V. PROSPECTS AT THE FUTURE COLLIDERS

The searches for a possible Higgs boson at ∼96 GeV will continue at ATLAS and CMS. However, it is not expected that such a particle could be seen in other decay modes than $\gamma\gamma$ and possibly $\tau^+\tau^-$. The pp environment makes it difficult to perform precision measurements of such a light Higgs boson. Better suited for such a task would be a future e^+e^- collider such as the planned ILC [22,25], where the light Higgs is produced in the Higgs-strahlung channel, $e^+e^- \to Z^* \to Zh_1$ [76–78]. The ILC can analyze the scenarios under investigation in two complementary ways. One can search for the new Higgs boson and analyze its properties directly. We also include, for the first time, an analysis of the coupling measurement of the h_1 at the ILC. On the other hand, one can perform precision measurements of the Higgs-boson at ∼125 GeV and look for indirect effects of the extended Higgs-boson sector. In this section we will explore both
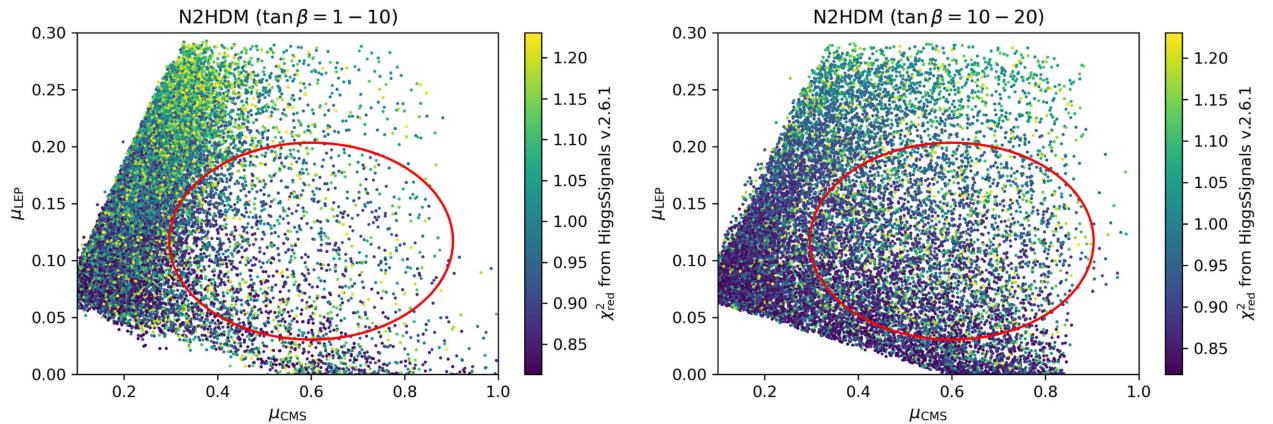
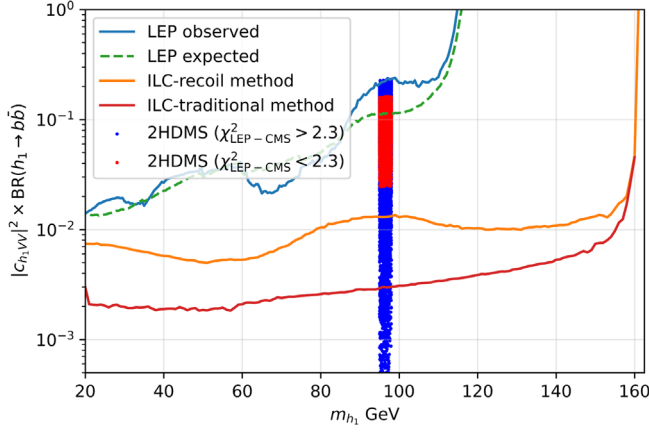FIG. 5. The N2HDM scan results with the same plane as in Fig. 1. The left (right) plot is for $\tan\beta = 1$–10 (10–20).

FIG. 6. The plane of m_{h_1} and S_{95}, which is defined as $\sigma(e^+e^- \to Zh_1)/\sigma_{SM} \times BR(h_1 \to b\bar{b})$. The green dashed (blue) line indicate the expected (observed) limits at LEP [10]. The orange and the red line show the reach of the ILC using the recoil method or the traditional method (see text). The red (blue) points indicate the parameter points within (outside of) the 1σ range of the 96 GeV excesses.

possibilities (where we will emphasize where we go beyond Refs. [22,25]). In particular, we analyze the 2HDMS and the N2HDM side-by-side to check for possible differences in their phenomenology.

A. Direct search for the 96 GeV Higgs boson

In Fig. 6 we show the plane of m_{h_1} and the quantity $|c_{h_1VV}|^2 \times BR(h_1 \to b\bar{b})$. The green dashed (blue) line indicates the expected (observed) limits at LEP [10], where the 2σ excess at ~96 GeV can be observed. The orange line and the red line show the reach of the ILC using the "recoil method" [79] or the "traditional method," see Ref. [76] for details (and Ref. [77] for a corresponding experimental analysis). This analysis assumed $\sqrt{s} = 250$ GeV and an

integrated luminosity of 500 fb^{-1}. The colored dots indicate the results from our parameter scan in the 2HDMS. The red (blue) points correspond to the parameter points inside (outside) the 1σ ellipse of μ_{CMS} and μ_{LEP}. One can observe that the red points, i.e. the ones describing the two excesses, are all well above the orange line. This shows that such light Higgs boson could be produced abundantly at the ILC. The same conclusion holds for the N2HDM.

In a second step we analyze the anticipated precision of the h_1 coupling measurements that can be performed at the ILC. We would like to stress that this constitutes the first analysis of this type: to which precision the couplings of a BSM Higgs boson can be measured at a future e^+e^- collider (all relevant details of this new analysis can be found in Appendix B), and what are the phenomenological consequences. Concretely, we assume an ILC center-of-mass energy of $\sqrt{s} = 250$ GeV and an integrated luminosity of 2 ab^{-1}. We concentrate on the points within the 1σ ellipse of the 96 GeV excesses in the $\mu_{CMS} - \mu_{LEP}$ plane. In Fig. 7 (left) we show the numbers of h_1 events produced in the Higgs-strahlung channel for the dominant decay modes. We directly compare the results for the 2HDMS and the N2HDM for the low and the high $\tan\beta$ region. It can be seen that no relevant differences can be observed, neither between the two models nor for the two $\tan\beta$ regions. It is remarkable that, depending on the channel, between ~10^3 and up to 10^5 events can be expected. The statistical uncertainty for these numbers is shown in the right plot of Fig. 7.

In the left plot of Fig. 8 we show the predictions for the effective couplings, which are the same for c_{h_1bb} and $c_{h_1\tau\tau}$, as well as for c_{h_1ZZ} and c_{h_1WW}. The only visible difference between the low and high $\tan\beta$ region is the somewhat enlarged range of c_{h_1tt}, which is found in the low $\tan\beta$ region. Naively, one would expect a corresponding enhancement in the number of gg events in the left plot of Fig. 7. However, the
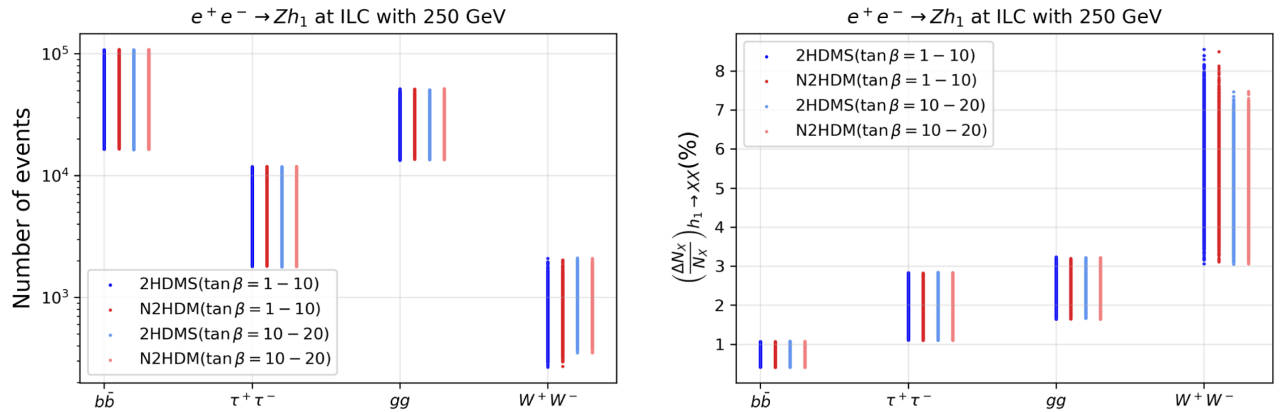

FIG. 7. Number of events (left) at the $h_1 \to b\bar{b}$, $h_1 \to \tau^+\tau^-$, $h_1 \to gg$ and $h_1 \to W^+W^-$ final states produced by the Higgs-strahlung process at the ILC, and the respective uncertainties (right) for the 2HDMS and the N2HDM scan points, which are within the 1σ ellipse of the 96 GeV excesses. The ILC center-of-mass energy is $\sqrt{s} = 250$ GeV and the integrated luminosity is 2 ab^{-1}.
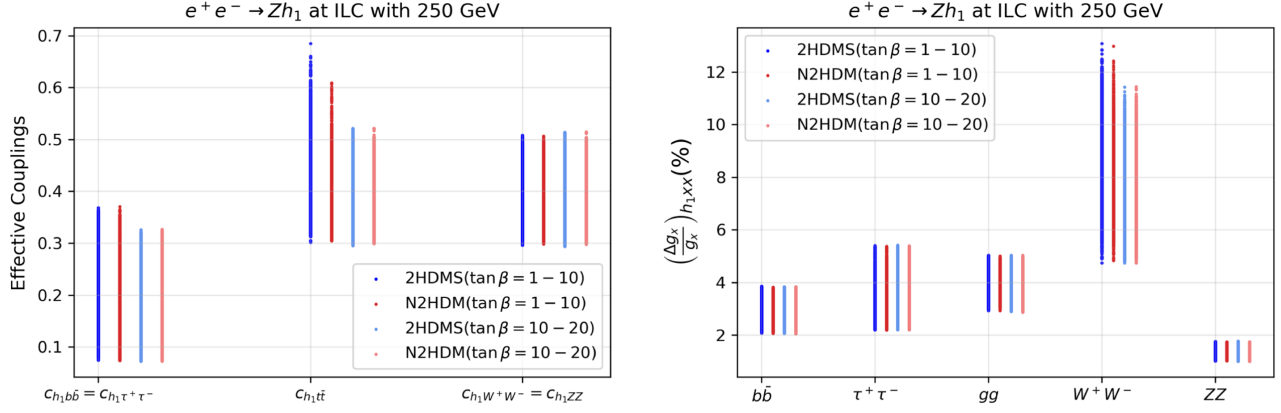
FIG. 8.   Left: the effective couplings of the h_1 for both 2HDMS and N2HDM in the two $\tan\beta$ regions. Right: the anticipated coupling measurement uncertainties (see text).

corresponding branching ratio is largely driven by the decay $h_1 \to b\bar{b}$, and no direct correspondence of $c_{h_1 tt}$ and BR($h_1 \to gg$) is found (see also the numbers for the best-fit points in Tables III and IV). Finally in the right plot of Fig. 8 we show a completely new type of analysis: the anticipated precision for the h_1 coupling measurement at the ILC (details about this evaluation are given in Appendix B). The coupling of the h_1 to $b\bar{b}$, $\tau^+\tau^-$, gg, and W^+W^- are determined from the respective decays, whereas the coupling to ZZ is determined from the Higgs-strahlung production. It is expected that the coupling of the h_1 to $b\bar{b}$ can be measured with an uncertainty between 2% and ~3.5%. For $\tau^+\tau^-$ and gg, the precision is expected to be only slightly worse. Because of the smaller coupling to W bosons, the corresponding uncertainty is found between ~4.5% and ~12%. The highest precision, however, is expected from the light Higgs-boson production via radiation from a Z boson, where an accuracy between 1% and 2% is anticipated. While these precisions are the same for the two models under investigation and as well as for the two $\tan\beta$ regions, they will nevertheless allow for a high-precision test of the 2HDMS/ N2HDM predictions. Concerning a possible differentiation of the two models, as before, we find that the different symmetries and couplings do not have any relevant impact on the h_1 coupling analysis. Consequently, in order to distinguish the 2HDMS and the N2HDM more direct phenomenological analyses will have to be performed, see our discussion in Sec. II D.

B. Measurement of the h_2 couplings

The Higgs boson observed at ~125 GeV at the LHC can also serve for the exploration of BSM models. The extended Higgs-boson sector of the 2HDMS/N2HDM, in particular the mixing of the lighter doublet with the singlet, yields deviations of the h_2 couplings from their SM expectations. In Fig. 9 we compare the predictions of the 2HDMS (blue points) and the N2HDM (red points) for

the effective h_2 couplings with the experimental accuracies. As before, special attention is paid to potential differences between the two models, leading possibly to an experimental distinction. Only points within the 1σ ellipse of the 96 GeV excesses are used, where the two $\tan\beta$ regions have been combined. Shown are $c_{h_2}bb$ vs $c_{h_2 tt}$ (upper left), $c_{h_2 VV}$ (upper right) and $c_{h_2\tau\tau}$ (lower plot). The black dotted (dashed) ellipses indicate the current ATLAS (CMS) 1σ limits (see Refs. [80,81]). The HL-LHC expectation [82], centered around the SM value, are shown as dashed violet ellipses. The orange (green) dashed ellipses indicate the improvements expected from the ILC at 250 GeV (additionally at 500 GeV), based on Ref. [83]. All the points are roughly within the 2σ range of the current Higgs-boson rate measurements at the LHC, because of the HIGGSSIGNALS constraint. No relevant difference between the two models can be observed. While $c_{h_2 bb} = c_{h_2\tau\tau}$ can reach the SM value (which by definition of the effective couplings is 1), the couplings to top quarks and to gauge bosons always deviate at least ~5% from the SM prediction. We have checked explicitly that this is due to the agreement with the 96 GeV excesses. For the coupling to top quarks, depending which point in the parameter space is realized, possibly no deviation can be observed, neither with the HL-LHC nor with the ILC precision. The situation is different for the h_2 coupling to gauge bosons. The HL-LHC precision might still yield a significance below the ~3σ level. The (in this case) strongly improved ILC precision, on the other hand, yields for all parameter points of the 2HDMS or the N2HDM a deviation from the SM prediction larger than 5σ. Consequently, the anticipated high-precision h_2 coupling measurements at the ILC will always either rule out the 2HDMS/N2HDM or refute the SM prediction. On the other hand, no distinction between the two models will be visible via the h_2 coupling determinations. This re-enforces our finding of the h_1 analysis in the previous subsection: only more direct phenomenological analyses will be able to
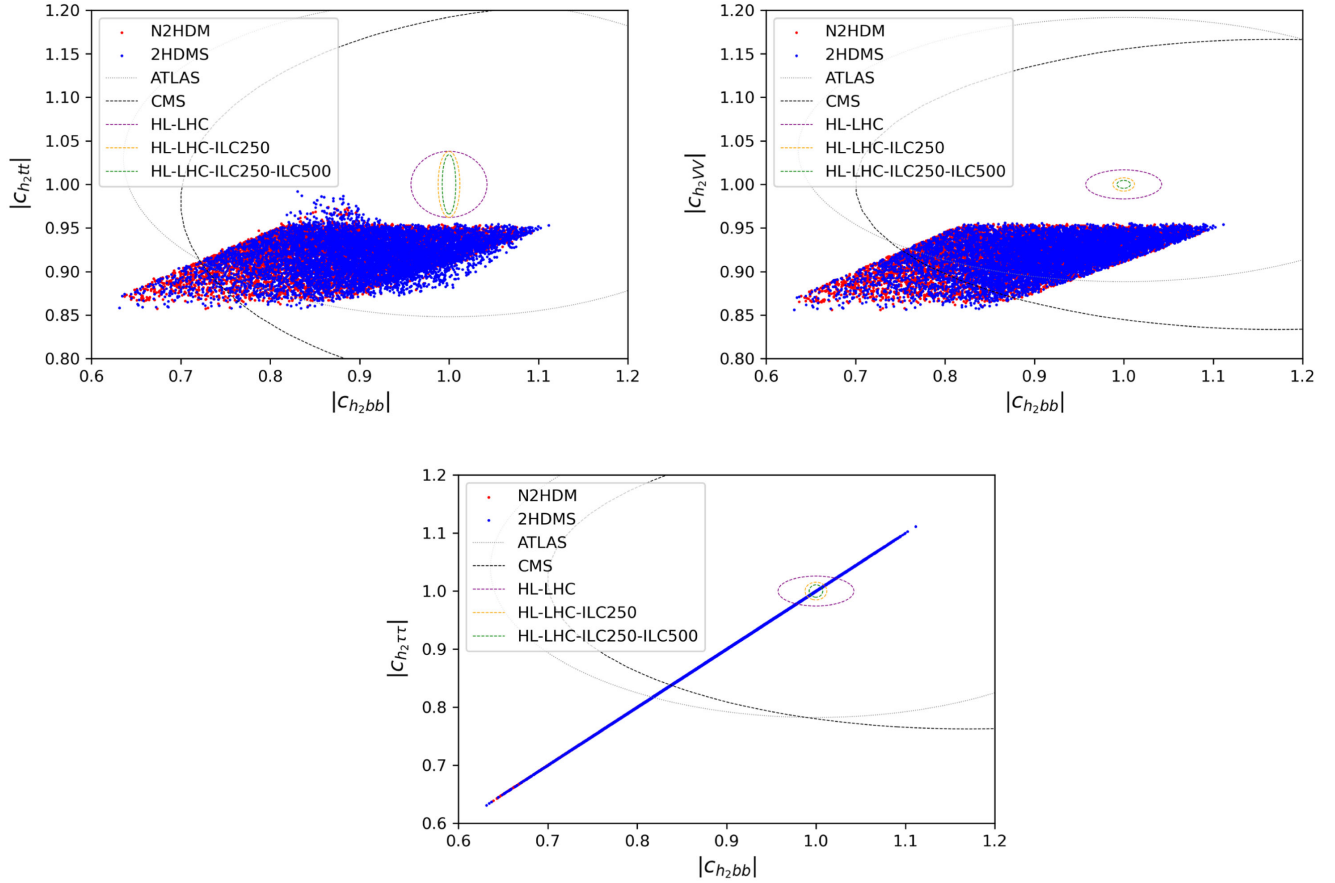
FIG. 9. The effective couplings of the SM-like Higgs-boson h_2. Shown are $|c_{h_2 bb}|$ vs $c_{h_2 tt}$ (upper left), $c_{h_2 VV}$ (upper right), and $c_{h_2 \tau\tau}$ (lower plot). The blue (red) points show the 2HDMS (N2HDM) points within the 1σ range of the 96 GeV excesses, with the two $\tan\beta$ ranges combined. The black dotted (dashed) ellipses indicate the current ATLAS (CMS) 1σ limits. The HL-LHC expectation, centered around the SM value, are shown as dashed violet ellipses. The orange (green) dashed ellipses indicate the improvements expected from the ILC at 250 GeV (additionally at 500 GeV).

distinguish the 2HDMS and the N2HDM, see our discussion in Sec. II D.

VI. CONCLUSIONS AND OUTLOOK

We analyzed a $\sim 3\sigma$ excess (local) in the diphoton decay mode at ~ 96 GeV as reported by CMS, together with a $\sim 2\sigma$ excess (local) in the $b\bar{b}$ final state at LEP in the same mass range. These two excesses can be interpreted as a new Higgs boson in extended SM models. Specifically we investigate the 2HDM type II with an additional singlet that can be either real (N2HDM) or complex (2HDMS). Besides the nature of the singlet, the two models differ in their symmetry structure. Both obey the $\mathbb{Z}_2$ symmetry present already in the 2HDM to avoid flavor changing neutral currents at the tree level. The N2HDM additionally obeys a second $\mathbb{Z}_2$ symmetry, while the 2HDMS obeys a $\mathbb{Z}_3$ symmetry such that this Higgs sector corresponds to the Higgs sectors of the NMSSM. In both models we have taken the lightest CP-even Higgs boson, h_1, at 96 GeV, while the second lightest, h_2, was set to 125 GeV. Special emphasis is paid to a possible experimental distinction between the two models. One main question we have investigated in this paper is whether the realization of a light Higgs boson at ~ 96 GeV in the two models, fitting the experimental excesses, leads to phenomenological consequences that eventually will allow us to differentiate between the 2HDMS and the N2HDM.

All relevant constraints are taken into account in our analysis. The first set are theoretical constraints from perturbativity and the requirement that the minimum of the Higgs potential is a stable global minimum. The second set are experimental constraints, where we take into account the direct searches for additional Higgs bosons from LEP. the Tevatron and the LHC, as well as the measurements of the properties of the Higgs boson at ~ 125 GeV. Furthermore, we include bounds from flavor physics and from electroweak precision data.

We find that both models, the 2HDMS and the N2HDM, can fit simultaneously the two excesses very well. For the 2HDMS this constitutes the first analysis of this type, while for the N2HDM our results can be seen as an update of

Ref. [22]. Concerning a possible experimental distinction between the two models, neither the different particle content nor the different symmetry structures have a relevant impact on how well the two models describe the excesses.

In a second step we have analyzed the couplings of the h_2 to SM fermions. In both models it was shown that in particular the coupling to gauge bosons differs substantially from its SM prediction. With the anticipated accuracy at the HL-LHC a $\sim 3\sigma$ effect would be visible. At a future e^+e^- collider, where concretely we employed ILC predictions, a signal at 5σ or more would be visible. On the other hand, also this analysis revealed no observable differences between the 2HDMS and the N2HDM.

In the final step of our analysis we analyzed with which precision the couplings of the 96 GeV Higgs boson could be measured at the ILC. This constitutes the first analysis of this type: to which precision the couplings of a BSM Higgs boson can be measured at a future e^+e^- collider (all relevant details of this new analysis can be found in Appendix B), and what are the phenomenological consequences. Concerning the results, the highest precision at the level of 1%–2% is expected for the $h_1 ZZ$ coupling, which is determined from the h_1 production in the Higgs-strahlung channel. Other coupling precisions are expected at the level of 2%–12%.

In all future coupling determinations no difference between the N2HDM and the 2HDMS was found, despite the different particle content and symmetry structure. Consequently, a distinction between the two models can be found only in analyses targeting more directly the different particle content and/or symmetry structure. The previous could manifest itself in the properties of the lighter *CP*-odd Higgs boson, which is always doubletlike in the N2HDM, but can be singletlike in the 2HDMS. The different symmetry structure has an impact on trilinear Higgs couplings. It could manifest itself concretely (in the model realizations we have analyzed) in the di-Higgs production (either at the HL-LHC or at a future e^+e^- collider) involving the lighter Higgs bosons. We leave both kinds of analyses for future work.

APPENDIX A: TREE-LEVEL HIGGS MASSES

In the following we discuss and compare the tree-level mixing matrices and physical basis in the N2HDM and the newly studied 2HDMS.

1. The 2HDMS

By taking the second derivative of the scalar potential, one can obtain the tree-level Higgs mass matrices:

$$M^2_{Sij} = \frac{\partial^2 V}{\partial \rho_i \partial \rho_j}\bigg|_{\substack{\Phi_1 = v_1 \\ \Phi_2 = v_2 \\ S = v_S}}, \qquad M^2_{Pij} = \frac{\partial^2 V}{\partial \eta_i \partial \eta_j}\bigg|_{\substack{\Phi_1 = v_1 \\ \Phi_2 = v_2 \\ S = v_S}},$$

$$M^2_{Cij} = \frac{\partial^2 V}{\partial \chi_i \partial \chi_j}\bigg|_{\substack{\Phi_1 = v_1 \\ \Phi_2 = v_2 \\ S = v_S}}. \tag{A1}$$

For the *CP*-even Higgs mass matrix one finds

$$M^2_{S11} = 2\lambda_1 v^2 \cos^2\beta + (m^2_{12} - \mu_{12} v_S) \tan\beta, \tag{A2a}$$

$$M^2_{S22} = 2\lambda_2 v^2 \sin^2\beta + (m^2_{12} - \mu_{12} v_S) \cot\beta, \tag{A2b}$$

$$M^2_{S12} = (\lambda_3 + \lambda_4) v^2 \sin 2\beta - (m^2_{12} - \mu_{12} v_S), \tag{A2c}$$

$$M^2_{S13} = (2\lambda'_1 v_S \cos\beta + \mu_{12} \sin\beta) v, \tag{A2d}$$

$$M^2_{S23} = (2\lambda'_2 v_S \sin\beta + \mu_{12} \cos\beta) v, \tag{A2e}$$

$$M^2_{S33} = \frac{\mu_{s1}}{2} v_S + \lambda''_3 v^2_S - \mu_{12} \frac{v^2}{2 v_S} \sin 2\beta. \tag{A2f}$$

The mass matrix of *CP*-odd Higgs sector is given by

$$M^2_{P11} = (m^2_{12} - \mu_{12} v_S) \tan\beta, \tag{A3a}$$

$$M^2_{P22} = (m^2_{12} - \mu_{12} v_S) \cot\beta, \tag{A3b}$$

$$M^2_{P12} = -(m^2_{12} - \mu_{12} v_S), \tag{A3c}$$

$$M^2_{P13} = \mu_{12} v \sin\beta, \tag{A3d}$$

$$M^2_{P23} = -\mu_{12} v \cos\beta, \tag{A3e}$$

$$M^2_{P33} = -\frac{3}{2} \mu_{S1} v_S - \mu_{12} \frac{v^2}{2 v_S} \sin 2\beta. \tag{A3f}$$

The charged Higgs-boson mass is obtained as

$$M^2_C = 2(m^2_{12} - \mu_{12} v_S) \csc 2\beta - \lambda_4 v^2. \tag{A4}$$

Since we parametrize the *CP*-even mixing matrix as the 3×3 rotation matrix R, see Eq. (11), one can perform the

diagonalization and express each mass-matrix element in terms of the mixing elements and the eigenvalues. In the CP-even Higgs-boson sector one has

$$M^2_{Sij} = \sum_{n=1}^{3} m^2_{h_n} R_{ni} R_{nj}. \tag{A5}$$

One can express the input parameters in terms of the Higgs-boson masses and mixing angles. Therefore we have the following relations to convert the input parameters in the original Lagrangian to the input parameters in the mass basis,

$$\mu_{12} = \frac{m^2_{a_2} - m^2_{a_1}}{v} \sin\alpha_4 \cos\alpha_4, \tag{A6}$$

$$v_S = \frac{m^2_{12} - \tilde{\mu}^2 \sin\beta\cos\beta}{\mu_{12}}, \tag{A7}$$

$$\mu_{S1} = -\frac{2}{3v_S} \left(\sin^2\alpha_4 m^2_{a_1} + \cos^2\alpha_4 m^2_{a_2} + \frac{v^2}{2v_S} \sin 2\beta \mu_{12} \right), \tag{A8}$$

$$\lambda_1 = \frac{1}{2v^2 \cos^2\beta} \left(\sum_i m^2_{h_i} R^2_{i1} - \tilde{\mu}^2 \sin^2\beta \right), \tag{A9}$$

$$\lambda_2 = \frac{1}{2v^2 \sin^2\beta} \left(\sum_i m^2_{h_i} R^2_{i2} - \tilde{\mu}^2 \cos^2\beta \right), \tag{A10}$$

$$\lambda_3 = \frac{1}{v^2} \left(\frac{1}{\sin 2\beta} \sum_i m^2_{h_i} R_{i1} R_{i2} + m^2_{h^\pm} - \frac{\tilde{\mu}^2}{2} \right), \tag{A11}$$

$$\lambda_4 = \frac{\tilde{\mu}^2 - m^2_{h^\pm}}{v^2}, \tag{A12}$$

$$\lambda'_1 = \frac{1}{2v_S v \cos\beta} \left(\sum_i m^2_{h_i} R_{i1} R_{i3} - \mu_{12} v \sin\beta \right), \tag{A13}$$

$$\lambda'_2 = \frac{1}{2v_S v \sin\beta} \left(\sum_i m^2_{h_i} R_{i2} R_{i3} - \mu_{12} v \cos\beta \right), \tag{A14}$$

$$\lambda''_3 = \frac{1}{v^2_S} \left(\sum_i m^2_{h_i} R^2_{i3} + \mu_{12} \frac{v^2}{2v_S} \sin 2\beta - \frac{\mu_{S1}}{2} v_S \right), \tag{A15}$$

where we define the parameter $\tilde{\mu}^2$ as

$$\tilde{\mu}^2 = \frac{m^2_{12} - v_S \mu_{12}}{\sin\beta\cos\beta} \equiv \cos^2\alpha_4 m^2_{a_1} + \sin^2\alpha_4 m^2_{a_2}. \tag{A16}$$

2. The N2HDM

The symmetric CP-even Higgs mass matrix in the N2HDM is obtained via a diagonalization with the same rotation matrix R in Eq. (11),

$$M^2_{S11} = 2\lambda_1 v^2 \cos^2\beta + m^2_{12} \tan\beta, \tag{A17a}$$

$$M^2_{S22} = 2\lambda_2 v^2 \sin^2\beta + m^2_{12} \cot\beta, \tag{A17b}$$

$$M^2_{S12} = (\lambda_3 + \lambda_4 + \lambda_5) v^2 \sin\beta\cos\beta - m^2_{12}, \tag{A17c}$$

$$M^2_{S13} = 2\lambda_7 v_S \cos\beta v, \tag{A17d}$$

$$M^2_{S23} = 2\lambda_8 v_S \sin\beta v. \tag{A17e}$$

$$M^2_{S33} = \lambda_6 v_S. \tag{A17f}$$

In the CP-odd sector the difference between the two models is characterized by the absence of a CP-odd mixing matrix due to the missing additional pseudoscalar-like Higgs in the N2HDM. In the scalar sector we have the same form as for the 2HDMS. In the 2HDMS we get additional terms containing μ_{12} and μ_{S1}, and the absence of of λ_5 enables the choice to use either v_s or m_{12} as an input parameter. However, by using the masses and mixing angles as input parameters, scalar Higgs masses and couplings to other SM particles would be effectively the same as in the N2HDM. Additional contributions will only be visible in the trilinear Higgs couplings and CP-odd sector (see Sec. II D).

One can perform a change of basis from the parameters of the potential to the physical masses and mixing angles similar to the 2HDMS. One finds

$$\lambda_1 = \frac{1}{v^2 \cos^2\beta} \left(\sum_i m^2_{h_i} R^2_{i1} - \hat{\mu}^2 \sin^2\beta \right), \tag{A18}$$

$$\lambda_2 = \frac{1}{v^2 \sin^2\beta} \left(\sum_i m^2_{h_i} R^2_{i2} - \hat{\mu}^2 \cos^2\beta \right), \tag{A19}$$

$$\lambda_3 = \frac{1}{v^2} \left(\frac{1}{\sin\beta\cos\beta} \sum_i m^2_{h_i} R_{i1} R_{i2} + 2m^2_{h^\pm} - \hat{\mu}^2 \right), \tag{A20}$$

$$\lambda_4 = \frac{1}{v^2} (\hat{\mu}^2 + m^2_A - 2m^2_{h^\pm}), \tag{A21}$$

$$\lambda_5 = \frac{1}{v^2} (\hat{\mu}^2 - m^2_A), \tag{A22}$$

$$\lambda_6 = \frac{1}{v^2_S} \sum_i m^2_{h_i} R^2_{i3}, \tag{A23}$$

$$\lambda_7 = \frac{1}{v v_S \cos\beta} \left(\sum_i m^2_{h_i} R_{i1} R_{i3} \right), \tag{A24}$$

$$\lambda_8 = \frac{1}{v v_S \sin\beta} \left(\sum_i m^2_{h_i} R_{i2} R_{i3} \right), \tag{A25}$$

where $\hat{\mu}^2$ is here defined as

$$\hat{\mu}^2 = \frac{m_{12}^2}{\sin\beta\cos\beta}. \tag{A26}$$

APPENDIX B: EVALUATION OF EXPERIMENTAL COUPLING UNCERTAINTIES FOR A LIGHT HIGGS BOSON

In this section we describe in detail how we estimate the experimental uncertainties of the coupling measurements of a Higgs boson below 125 GeV based on ILC250 measurements. We would like to stress that this constitutes the first analysis of this type: to which precision the couplings of a BSM Higgs boson can be measured at a future e^+e^- collider. This facilitates future phenomenological analysis that may allow to obtain information about the underlying model and its preferred parameter space.

1. SM Higgs-boson results

In this subsection we denote the SM Higgs boson as h and assume a mass of 125 GeV. The cross section at the ILC250 is given as

$$\sigma(e^+e^- \to Zh) = 206 \text{ fb}. \tag{B1}$$

The BRs are taken from Ref. [84] and summarized in Table V.

The SH Higgs coupling uncertainties have been obtained in Ref. [85] (Table II), assuming $\mathcal{L}_{\text{int}} = 2 \text{ ab}^{-1}$ at $\sqrt{s} = 250$ GeV (i.e. the ILC250). The results are given in Table VI.

The numbers for the ratio of signal over background events, $S/B(=: f_h)$ of a SM Higgs boson at 125 GeV at the ILC250 are given in Table VII [86]. The hZZ coupling is determined directly from the cross section, where the $q\bar{q}h$ mode can be neglected. The other couplings should be taken in the $q\bar{q}h$ mode, corresponding effectively to $e^+e^- \to Z^* \to Zh \to q\bar{q}h$ (with the subsequent Higgs decay).

TABLE V.   BRs of the SM Higgs boson [84].

Final state	$b\bar{b}$	$c\bar{c}$	gg	$\tau^+\tau^-$	WW^*
BR	0.582	0.029	0.082	0.063	0.214

TABLE VI.   Relative uncertainties in the SM Higgs couplings, $\Delta g_x/g_x$, at the ILC250 [85].

Coupling	$b\bar{b}$	$c\bar{c}$	gg	$\tau^+\tau^-$	WW	ZZ
Relative uncertainties [%]	1.04	1.79	1.60	1.16	0.65	0.66

TABLE VII.   Numbers for S/B at the ILC250 [86].

Measurement	Efficiency	S/B
σ_{Zh} in $\mu^+\mu^-h$	88%	1/1.3
σ_{Zh} in e^+e^-h	68%	1/2.0
BR($h \to b\bar{b}$) in $q\bar{q}h$	33%	1/0.89
BR($h \to c\bar{c}$) in $q\bar{q}h$	26%	1/4.7
BR($h \to gg$) in $q\bar{q}h$	26%	1/13
BR($h \to \tau^+\tau^-$) in $q\bar{q}h$	37%	1/0.44
BR($h \to WW$) in $q\bar{q}h$	2.6%	1/0.96

2. Basic signal-background statistics

In this section we use the following notation: $N_S(\equiv S)$: number of signal events; $N_B(\equiv B)$: number of background events; N_T: total number of events with. Then one finds

$$N_S = N_T - N_B, \tag{B2}$$

$$f = N_S/N_B. \tag{B3}$$

The background is taken after cuts, i.e. "irreducible background," likely to be small at an e^+e^- collider. For the uncertainties we have

$$\Delta N_S^2 = \Delta N_T^2 + \Delta N_B^2. \tag{B4}$$

The uncertainty of the total number of events scales like

$$\Delta N_T = \sqrt{N_T}. \tag{B5}$$

The uncertainty of the background goes like

$$\Delta N_B = \epsilon_{\text{syst},B} \cdot N_B, \tag{B6}$$

where $\epsilon_{\text{syst},B}$ denotes the relative uncertainty for background estimation (which cancels out later). Therefore,

$$\Delta N_S^2 = (\sqrt{N_T})^2 + (\epsilon_{\text{syst},B} \cdot N_B)^2, \tag{B7}$$

$$\Delta N_S = \sqrt{(N_S + N_B) + \epsilon_{\text{syst},B}^2 N_B^2}. \tag{B8}$$

If the background is known perfectly, one has overall uncertainty fully dominated by the purely statistical uncertainty,

$$\epsilon_{\text{syst},B} = 0, \tag{B9}$$

$$\begin{aligned} \Delta N_S &= \sqrt{N_S + N_B} \\ &= \sqrt{N_S + N_S/f} \\ &= \sqrt{N_S(1 + 1/f)} \\ &= \sqrt{N_S} \cdot \sqrt{1 + 1/f}, \end{aligned} \tag{B10}$$

$$\Delta N_S/N_S = \frac{1}{\sqrt{N_S}} \cdot \sqrt{1 + 1/f}. \qquad \text{(B11)}$$

Consequently, the uncertainty improves with $\sqrt{N_S}$ if $f = N_S/N_B \gg 1$. On the other hand, if f is small, one wins less from the gain in statistics.

3. Evaluation of uncertainties in the Higgs couplings

a. Cross section evaluation

The production cross section for a Higgs ϕ at an e^+e^- collider is evaluated as

$$\sigma(e^+e^- \to \phi Z) = \sigma_{\mathrm{SM}}(e^+e^- \to H_{\mathrm{SM}}^\phi Z) \times |c_{\phi VV}|^2. \qquad \text{(B12)}$$

Here H_{SM}^ϕ is the SM Higgs boson with a hypothetical mass equal to m_ϕ. $c_{\phi VV}$ is the coupling strength of the ϕ to two gauge bosons ($V = W^\pm, Z$) relative to the SM value. In Fig. 10 we show the evaluation of $\sigma_{\mathrm{SM}}(e^+e^- \to H_{\mathrm{SM}}^\phi Z)$ (where H_{SM}^ϕ is labeled H) at the tree level ("tree") and the full one-loop level ("full") [87], including soft and hard QED radiation. One can see that the loop corrections are important for the reliable evaluation of this cross section. Explicit numbers are given in Table VIII. Multiplying the loop corrected cross section with $|c_{\phi VV}|^2$ is an approximation that works well for $m_\phi \gtrsim 75$ GeV and requires more scrutiny for the lowest Higgs-boson masses.
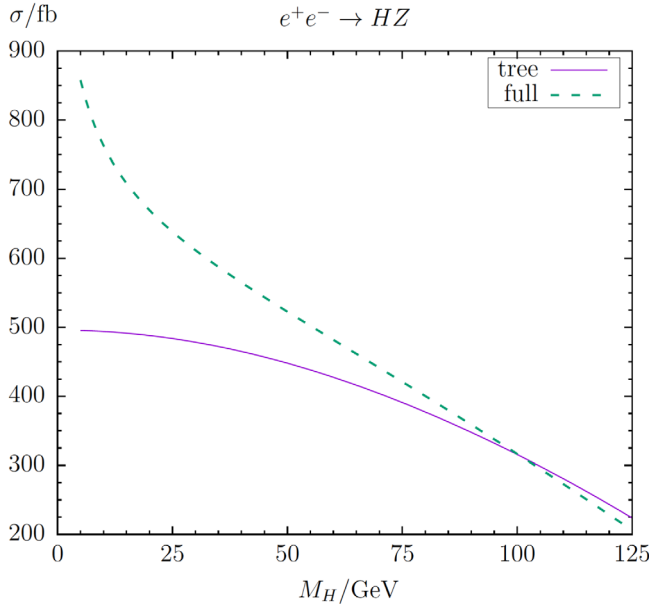

FIG. 10. Production cross section for "SM Higgs bosons" with $m_H \leq 125$ GeV [87].

b. Signal over background for the new Higgs boson

An important element for the evaluation of the Higgs-boson coupling uncertainties is the number of signal over background events for ϕ,

$$\left(\frac{N_S}{N_B}\right)_\phi =: f_\phi \qquad \text{(B13)}$$

relative to the SM value(s) as given in Table VII,

$$\left(\frac{N_S}{N_B}\right)_h =: f_h \qquad \text{(B14)}$$

with

$$\left(\frac{N_S}{N_B}\right)_h \Big/ \left(\frac{N_S}{N_B}\right)_\phi = f_h/f_\phi =: D. \qquad \text{(B15)}$$

Unfortunately, there is no (neither general nor model specific) evaluation of f_ϕ or D available. However, for the ILC500 "SM-like" Higgs bosons with masses above and below 125 GeV have been simulated [78]. One finds that in this case very roughly $D \approx 2$ can be assumed. For our evaluation we use $D = 3$ as a conservative value.

c. Relating signal events to Higgs couplings

In this subsection we derive the evaluation of the uncertainties in the (light) Higgs-boson couplings. We denote the generic coupling of a Higgs ϕ to another particle x as g_x. There are two cases:

(i) The coupling is determined via the decay $\phi \to xx$. The number of signal events is given by

$$N_S = \mathcal{L}_{\mathrm{int}} \times \sigma(e^+e^- \to \phi Z) \times \mathrm{BR}(\phi \to xx) \\ \times \epsilon_{\mathrm{sel}} \times \mathrm{BR}(Z \to q\bar{q}), \qquad \text{(B16)}$$

$$\mathrm{BR}(\phi \to xx) = \frac{\Gamma(\phi \to xx)}{\Gamma_{\mathrm{tot}}}, \qquad \text{(B17)}$$

where ϵ_{sel} is the selection efficiency. In the formulas below ϵ_{sel} and $\mathrm{BR}(Z \to q\bar{q})$ cancel out, but they enter in the N_S/N_B evaluation, i.e. in the numbers of S/B given in Table VII, as well as in the coupling precisions given in Table VI. The decay channel $\phi \to xx$ gives not only $\Gamma(\phi \to xx)$, but also contributes to Γ_{tot}. For simplicity we assume

$$\mathrm{BR}(\phi \to xx) = \frac{g_x^2}{g_x^2 + g^2}, \qquad \text{(B18)}$$

where g^2 (modulo canceled prefactors) summarizes the other contributions. The relative strength between g_x and g is given by

TABLE VIII.   Production cross section for "SM Higgs bosons" with $m_\phi \equiv m_H \leq 125$ GeV [87].

m_ϕ [GeV]	5	10	20	30	40	50	60	70	80	90	96	100	110	120
σ_{HZ} [fb]	858	763	670	611	565	523	482	441	400	359	333	316	273	228

$$(p-1)g_x^2 = g^2, \tag{B19}$$

$$\Rightarrow \mathrm{BR}(\phi \to xx) = \frac{1}{p}. \tag{B20}$$

Then one finds

$$N_S + \Delta N_S \propto \mathrm{BR} + \Delta \mathrm{BR}$$

$$= \frac{g_x^2(1 + \Delta g_x/g_x)^2}{g_x^2(1 + \Delta g_x/g_x)^2 + (p-1)g_x^2}$$

$$= \frac{1}{p}\left(1 + 2\frac{\Delta g_x}{g_x} - 2\frac{\Delta g_x}{g_x p}\right) \tag{B21}$$

$$\Rightarrow \Delta \mathrm{BR} = \frac{1}{p}\left(2\frac{\Delta g_x}{g_x} - 2\frac{\Delta g_x}{g_x p}\right), \tag{B22}$$

$$\Rightarrow \frac{\Delta N_S}{N_S} = \frac{\Delta \mathrm{BR}}{\mathrm{BR}} = 2\frac{\Delta g_x}{g_x} - 2\frac{\Delta g_x}{g_x p}$$

$$= 2\frac{\Delta g_x}{g_x}\left(1 - \frac{1}{p}\right). \tag{B23}$$

(ii) The coupling is determined via the production cross section. This is the case for g_Z.

Then one can assume [where as above the $\mathrm{BR}(Z \to \ell^+\ell^-)$ cancels out]

$$N_S \propto \sigma(e^+e^- \to \phi Z) \times \mathrm{BR}(Z \to e^+e^-, \mu^+\mu^-) \propto g_Z^2, \tag{B24}$$

$$N_S + \Delta N_S \propto (g_Z + \Delta g_Z)^2. \tag{B25}$$

$$\Delta N_S/N_S \propto 2\frac{\Delta g_Z}{g_Z}. \tag{B26}$$

d. Uncertainty in the Higgs couplings

In the following we denote the SM Higgs boson as h, and the new Higgs boson at 96 GeV as ϕ. For the SM Higgs boson we have

(i) $\sigma(e^+e^- \to Zh)$ from Eq. (B1) and $\mathrm{BR}(h \to xx)$ from Table V, which gives us $N_{S,h}$.

(ii) $\left(\frac{N_S}{N_B}\right)_h$ from Table VII.

This allows us to evaluate $\left(\frac{\Delta N_S}{N_S}\right)_h$ via Eq. (B11).

(iii) $\left(\frac{\Delta g_x}{g_x}\right)_h$ from Table VI.

For the new Higgs boson ϕ we have

(i) $N_{S,\phi}$ from Eq. (B16).

(ii) For $\left(\frac{N_S}{N_B}\right)_\phi$ we assume $f_h/f_\phi = D$ with $D = 2$ as a starting/central point.

This allows us to evaluate $\left(\frac{\Delta N_S}{N_S}\right)_\phi$ via Eq. (B11).

Here it should be kept in mind that D is *a priori* unknown. We use, as discussed above, $D = 3$ as a conservative value.

Using the proportionality relations one can evaluate the coupling precision in the two cases:

(i) The coupling determined via the decay $\phi \to xx$. Here one finds

$$\frac{\left(\frac{\Delta g_x}{g_x}\right)_\phi}{\left(\frac{\Delta g_x}{g_x}\right)_h} = \frac{\left(\frac{\Delta N_S}{N_S}\right)_\phi}{\left(\frac{\Delta N_S}{N_S}\right)_h} \times \frac{(1 - \frac{1}{p_h})}{(1 - \frac{1}{p_\phi})} \tag{B27}$$

and can thus evaluate $\left(\frac{\Delta g_x}{g_x}\right)_\phi$ using

$$\frac{\left(\frac{\Delta N_S}{N_S}\right)_\phi}{\left(\frac{\Delta N_S}{N_S}\right)_h} \times \frac{(1 - \frac{1}{p_h})}{(1 - \frac{1}{p_\phi})} = \frac{\left(\frac{\sqrt{1+1/f_\phi}}{\sqrt{N_{S,\phi}}}\right)}{\left(\frac{\sqrt{1+1/f_h}}{\sqrt{N_{S,h}}}\right)} \times \frac{(1 - \frac{1}{p_h})}{(1 - \frac{1}{p_\phi})} \tag{B28}$$

$$= \frac{\sqrt{1 + D/f_h}}{\sqrt{1 + 1/f_h}} \times \frac{\sqrt{N_{S,h}}}{\sqrt{N_{S,\phi}}} \times \frac{(1 - \mathrm{BR}(h \to xx))}{(1 - \mathrm{BR}(\phi \to xx))} \tag{B29}$$

$$= \sqrt{\frac{D + f_h}{1 + f_h}} \times \sqrt{\frac{\sigma(e^+e^- \to Zh)}{\sigma(e^+e^- \to Z\phi)}} \times \sqrt{\frac{\mathrm{BR}(h \to xx)}{\mathrm{BR}(\phi \to xx)}}$$

$$\times \frac{(1 - \mathrm{BR}(h \to xx))}{(1 - \mathrm{BR}(\phi \to xx))}. \tag{B30}$$

(ii) The coupling is determined via the production cross section, i.e. g_Z. Here we find

$$\frac{\left(\frac{\Delta g_Z}{g_Z}\right)_\phi}{\left(\frac{\Delta g_Z}{g_Z}\right)_h} = \frac{\left(\frac{\Delta N_S}{N_S}\right)_\phi}{\left(\frac{\Delta N_S}{N_S}\right)_h} \tag{B31}$$

and can thus evaluate $\left(\frac{\Delta g_Z}{g_Z}\right)_\phi$ using

$$\frac{\left(\frac{\Delta N_S}{N_S}\right)_\phi}{\left(\frac{\Delta N_S}{N_S}\right)_h} = \frac{\sqrt{N_{S,h}}}{\sqrt{N_{S,\phi}}} \tag{B32}$$

$$= \sqrt{\frac{\sigma(e^+e^- \to Zh)}{\sigma(e^+e^- \to Z\phi)}}. \tag{B33}$$

[1] Georges Aad *et al.*, Observation of a new particle in the search for the Standard Model Higgs boson with the ATLAS detector at the LHC, Phys. Lett. B **716,** 1 (2012).

[2] Serguei Chatrchyan *et al.*, Observation of a new boson at a mass of 125 GeV with the CMS experiment at the LHC, Phys. Lett. B **716,** 30 (2012).

[3] Georges Aad *et al.*, Measurements of the Higgs boson production and decay rates and constraints on its couplings from a combined ATLAS and CMS analysis of the LHC pp collision data at $\sqrt{s} = 7$ and 8 TeV, J. High Energy Phys. 08 (2016) 045.

[4] Jeremy Bernon, John F. Gunion, Yun Jiang, and Sabine Kraml, Light Higgs bosons in two-Higgs-doublet models, Phys. Rev. D **91,** 075019 (2015).

[5] Tania Robens and Tim Stefaniak, Status of the Higgs singlet extension of the standard model after LHC run 1, Eur. Phys. J. C **75,** 104 (2015).

[6] S. Heinemeyer, O. Stal, and G. Weiglein, Interpreting the LHC Higgs search results in the MSSM, Phys. Lett. B **710,** 201 (2012).

[7] Florian Domingo and Georg Weiglein, NMSSM interpretations of the observed Higgs signal, J. High Energy Phys. 04 (2016) 095.

[8] Philip Bechtle, Howard E. Haber, Sven Heinemeyer, Oscar Stål, Tim Stefaniak, Georg Weiglein, and Lisa Zeune, The light and heavy Higgs interpretation of the MSSM, Eur. Phys. J. C **77,** 67 (2017).

[9] G. Abbiendi *et al.*, Decay mode independent searches for new scalar bosons with the OPAL detector at LEP, Eur. Phys. J. C **27,** 311 (2003).

[10] R. Barate *et al.*, Search for the standard model Higgs boson at LEP, Phys. Lett. B **565,** 61 (2003).

[11] S. Schael *et al.*, Search for neutral MSSM Higgs bosons at LEP, Eur. Phys. J. C **47,** 547 (2006).

[12] CDF, D0, Updated combination of CDF and D0 searches for Standard Model Higgs boson production with up to 10.0 fb^{-1} of data, Report No. FERMILAB-CONF-12-318-E, CDF-NOTE-10884, D0-NOTE-6348 (2012), arXiv:1207.0449.

[13] CMS, Search for new resonances in the diphoton final state in the mass range between 70 and 110 GeV in pp collisions at $\sqrt{s} = 8$ and 13 TeV, Report No. CMS-PAS-HIG-17-013 (2017).

[14] Albert M. Sirunyan *et al.*, Search for a standard model-like Higgs boson in the mass range between 70 and 110 GeV in the diphoton final state in proton-proton collisions at $\sqrt{s} = 8$ and 13 TeV, Phys. Lett. B **793,** 320 (2019).

[15] Albert M. Sirunyan *et al.*, Search for additional neutral MSSM Higgs bosons in the $\tau\tau$ final state in proton-proton collisions at $\sqrt{s} = 13$ TeV, J. High Energy Phys. 09 (2018) 007.

[16] ATLAS, Search for resonances in the 65 to 110 GeV diphoton invariant mass range using 80 fb^{-1} of pp collisions collected at $\sqrt{s} = 13$ TeV with the ATLAS detector, Report No. ATLAS-CONF-2018-025 (2018).

[17] CMS, Search for new resonances in the diphoton final state in the mass range between 80 and 115 GeV in pp collisions at $\sqrt{s} = 8$ TeV, Report No. CMS-PAS-HIG-14-037 (2015).

[18] Sven Heinemeyer and T. Stefaniak, A Higgs boson at 96 GeV?!, Proc. Sci. CHARGED2018 (**2019**) 016.

[19] S. Heinemeyer, A Higgs boson below 125 GeV?!, Int. J. Mod. Phys. A **33,** 1844006 (2018).

[20] François Richard, Indications for extra scalars at LHC?—+BSM physics at future e^+e^- colliders (2020), arXiv:2001.04770.

[21] T. Biekötter, M. Chakraborti, and S. Heinemeyer, The "96 GeV excess" at the LHC (2020).

[22] T. Biekötter, M. Chakraborti, and S. Heinemeyer, A 96 GeV Higgs boson in the N2HDM, Eur. Phys. J. C **80,** 2 (2020).

[23] Thomas Biekötter, M. Chakraborti, and Sven Heinemeyer, An N2HDM solution for the possible 96 GeV excess, Proc. Sci. CORFU2018 (**2019**) 015.

[24] T. Biekötter, M. Chakraborti, and S. Heinemeyer, The "96 GeV excess" in the N2HDM, in *Proceedings of 31st Rencontres de Blois on Particle Physics and Cosmology* (2019), arXiv:1910.06858.

[25] T. Biekötter, M. Chakraborti, and S. Heinemeyer, The "96 GeV excess" at the ILC, in *Proceedings of International Workshop on Future Linear Colliders* (2020), arXiv:2002.06904.

[26] Thomas Biekötter, Alexander Grohsjean, Sven Heinemeyer, Christian Schwanenberger, and Georg Weiglein, Possible indications for new Higgs bosons in the reach of the LHC: N2HDM and NMSSM interpretations, Eur. Phys. J. C **82,** 178 (2022).

[27] Florian Domingo, Sven Heinemeyer, Sebastian Paßehr, and Georg Weiglein, Decays of the neutral Higgs bosons into SM fermions and gauge bosons in the $\mathcal{CP}$-violating NMSSM, Eur. Phys. J. C **78,** 942 (2018).

[28] Kiwoon Choi, Sang Hui Im, Kwang Sik Jeong, and Chan Beom Park, Light Higgs bosons in the general NMSSM, Eur. Phys. J. C **79,** 956 (2019).

[29] T. Biekötter, S. Heinemeyer, and C. Muñoz, Precise prediction for the Higgs-boson masses in the $\mu\nu$ SSM, Eur. Phys. J. C **78,** 504 (2018).

[30] T. Biekötter, S. Heinemeyer, and C. Muñoz, Precise prediction for the Higgs-boson masses in the $\mu\nu$ SSM with three right-handed neutrino superfields, Eur. Phys. J. C **79,** 667 (2019).

[31] Wolfgang Gregor Hollik, Stefan Liebler, Gudrid Moortgat-Pick, Sebastian Paßehr, and Georg Weiglein, Phenomenology of the inflation-inspired NMSSM at the electroweak scale, Eur. Phys. J. C **79,** 75 (2019).

[32] Junjie Cao, Xinglong Jia, Yuanfang Yue, Haijing Zhou, and Pengxuan Zhu, 96 GeV diphoton excess in seesaw extensions of the natural NMSSM, Phys. Rev. D **101,** 055008 (2020).

[33] Patrick J. Fox and Neal Weiner, Light signals from a lighter Higgs, J. High Energy Phys. 08 (2018) 025.

[34] Ulrich Haisch and Augustinas Malinauskas, Let there be light from a second light Higgs doublet, J. High Energy Phys. 03 (2018) 135.

[35] Thomas Biekötter and María Olalla Olea-Romacho, Reconciling Higgs physics and pseudo-Nambu-Goldstone dark matter in the S2HDM using a genetic algorithm, J. High Energy Phys. 10 (2021) 215.

[36] Francois Richard, Search for a light radion at HL-LHC and ILC250, Report No. LAL-17-060 (2017), arXiv:1712.06410.

[37] Da Liu, Jia Liu, Carlos E. M. Wagner, and Xiao-Ping Wang, A light Higgs at the LHC and the B-anomalies, J. High Energy Phys. 06 (2018) 150.

[38] Lijia Liu, Haoxue Qiao, Kun Wang, and Jingya Zhu, A light scalar in the minimal dilaton model in light of LHC constraints, Chin. Phys. C **43**, 023104 (2019).

[39] James M. Cline and Takashi Toma, Pseudo-Goldstone dark matter confronts cosmic ray and collider anomalies, Phys. Rev. D **100**, 035023 (2019).

[40] Juan Antonio Aguilar-Saavedra and Filipe Rafael Joaquim, Multiphoton signals of a (96 GeV?) stealth boson, Eur. Phys. J. C **80**, 403 (2020).

[41] Chien-Yi Chen, Michael Freid, and Marc Sher, Next-to-minimal two Higgs doublet model, Phys. Rev. D **89**, 075009 (2014).

[42] Margarete Muhlleitner, Marco O. P. Sampaio, Rui Santos, and Jonas Wittbrodt, The N2HDM under theoretical and experimental scrutiny, J. High Energy Phys. 03 (2017) 094.

[43] Isabell Engeln, Pedro Ferreira, M. Margarete Mühlleitner, Rui Santos, and Jonas Wittbrodt, The dark phases of the N2HDM, J. High Energy Phys. 08 (2020) 085.

[44] G. C. Branco, P. M. Ferreira, L. Lavoura, M. N. Rebelo, Marc Sher, and Joao P. Silva, Theory and phenomenology of two-Higgs-doublet models, Phys. Rep. **516**, 1 (2012).

[45] Sebastian Baum and Nausheen R. Shah, Two Higgs doublets and a complex singlet: Disentangling the decay topologies and associated phenomenology, J. High Energy Phys. 12 (2018) 044.

[46] Margarete Mühlleitner, Marco O. P. Sampaio, Rui Santos, and Jonas Wittbrodt, Scanners: Parameter scans in extended scalar sectors, Eur. Phys. J. C **82**, 198 (2022).

[47] J. Horejsi and M. Kladiva, Tree-unitarity bounds for THDM Higgs masses revisited, Eur. Phys. J. C **46**, 81 (2006).

[48] K. G. Klimenko, On necessary and sufficient conditions for some Higgs potentials to be bounded from below, Theor. Math. Phys. **62**, 58 (1985).

[49] P. M. Ferreira, Rui Santos, Margarete Mühlleitner, Georg Weiglein, and Jonas Wittbrodt, Vacuum instabilities in the N2HDM, J. High Energy Phys. 09 (2019) 006.

[50] Wolfgang G. Hollik, Georg Weiglein, and Jonas Wittbrodt, Impact of vacuum stability constraints on the phenomenology of supersymmetric models, J. High Energy Phys. 03 (2019) 109.

[51] J. Wittbrodt, https://gitlab.com/jonaswittbrodt/EVADE.

[52] Tsung-Lin Lee, Tien-Yien Li, and Chih-Hsiung Tsai, Hom4 ps-2.0: A software package for solving polynomial systems by the polyhedral homotopy continuation method, Computing **83**, 109 (2008).

[53] Victor Guada, Miha Nemevšek, and Matevž Pintar, Findbounce: Package for multi-field bounce actions, Comput. Phys. Commun. **256**, 107480 (2020).

[54] J. Eliel, https://github.com/JoseEliel/VevaciousPlusPlus_Development.

[55] J. E. Camargo-Molina, B. O'Leary, W. Porod, and F. Staub, Vevacious: A tool for finding the global minima of one-loop effective potentials with many scalars, Eur. Phys. J. C **73**, 2588 (2013).

[56] Philip Bechtle, Sven Heinemeyer, Oscar Stål, Tim Stefaniak, and Georg Weiglein, HiggsSignals: Confronting arbitrary Higgs sectors with measurements at the Tevatron and the LHC, Eur. Phys. J. C **74**, 2711 (2014).

[57] Philip Bechtle, Sven Heinemeyer, Oscar Stål, Tim Stefaniak, and Georg Weiglein, Probing the Standard Model with Higgs signal rates from the Tevatron, the LHC and a future ILC, J. High Energy Phys. 11 (2014) 039.

[58] Philip Bechtle, Oliver Brein, Sven Heinemeyer, Georg Weiglein, and Karina E. Williams, HiggsBounds: Confronting arbitrary Higgs sectors with exclusion bounds from LEP and the Tevatron, Comput. Phys. Commun. **181**, 138 (2010).

[59] Philip Bechtle, Oliver Brein, Sven Heinemeyer, Georg Weiglein, and Karina E. Williams, HiggsBounds 2.0.0: Confronting neutral and charged Higgs sector predictions with exclusion bounds from LEP and the Tevatron., Comput. Phys. Commun. **182**, 2605 (2011).

[60] Philip Bechtle, Oliver Brein, Sven Heinemeyer, Oscar Stål, Tim Stefaniak, Georg Weiglein, and Karina E. Williams, HiggsBounds – 4: Improved tests of extended Higgs sectors against exclusion bounds from LEP, the Tevatron and the LHC, Eur. Phys. J. C **74**, 2693 (2014).

[61] Philip Bechtle, Sven Heinemeyer, Oscar Stal, Tim Stefaniak, and Georg Weiglein, Applying exclusion likelihoods from LHC searches to extended Higgs sectors, Eur. Phys. J. C **75**, 421 (2015).

[62] A. Arbey, F. Mahmoudi, O. Stal, and T. Stefaniak, Status of the charged Higgs boson in two Higgs doublet models, Eur. Phys. J. C **78**, 182 (2018).

[63] M. Aaboud, G. Aad, B. Abbott, O. Abdinov, B. Abeloos, D. K. Abhayasinghe, S. H. Abidi, O. S. AbouZeid, N. L. Abraham *et al.*, Search for charged Higgs bosons decaying into top and bottom quarks at $\sqrt{s} = 13$ TeV with the Atlas detector, J. High Energy Phys. 06 (2021) 145.

[64] M. Ciuchini, G. Degrassi, P. Gambino, and G. F. Giudice, Next-to-leading QCD corrections to $b \rightarrow xs\gamma$: Standard model and two-Higgs doublet model, Nucl. Phys. **B527**, 21 (1998).

[65] Thomas Hermann, Mikolaj Misiak, and Matthias Steinhauser, $\bar{B} \rightarrow X_s\gamma$ in the two Higgs doublet model up to next-to-next-to-leading order in QCD, J. High Energy Phys. 11 (2012) 036.

[66] M. Misiak, H. Asatrian, R. Boughezal, M. Czakon, T. Ewerth, A. Ferroglia, P. Fiedler, P. Gambino, C. Greub, U. Haisch *et al.*, Updated Next-to-Next-to-Leading-Order QCD Predictions for the Weak Radiative B-Meson Decays, Phys. Rev. Lett. **114**, 221801 (2015).

[67] Qin Chang, Pei-Fu Li, and Xin-Qiang Li, B_s^0-$\bar{B}_s^0$ mixing within minimal flavor-violating two-Higgs-doublet models, Eur. Phys. J. C **75**, 594 (2015).

[68] T. Barakat, The rare decay $k \rightarrow \pi\nu\nu$ in two Higgs doublet model in two Higgs doublet model, Il Nuovo Cimento A **112**, 697 (1999).

[69] W. Grimus, L. Lavoura, O. M. Ogreid, and P. Osland, The oblique parameters in multi-Higgs-doublet models, Nucl. Phys. **B801**, 81 (2008).

[70] Junjie Cao, Xiaofei Guo, Yangle He, Peiwen Wu, and Yang Zhang, Diphoton signal of the light Higgs boson in natural NMSSM, Phys. Rev. D **95**, 116001 (2017).

[71] S. Gascon-Shotkin, Update on Higgs searches below 125 GeV, in Higgs Days at Sandander (2017), https://indico.cern.ch/event/666384/contributions/2723427/.

[72] Werner Porod, SPheno, a program for calculating supersymmetric spectra, SUSY particle decays and SUSY particle production at e^+e^- colliders, Comput. Phys. Commun. **153,** 275 (2003).

[73] W. Porod and F. Staub, SPheno 3.1: Extensions including flavour, *CP*-phases and models beyond the MSSM, Comput. Phys. Commun. **183,** 2458 (2012).

[74] Florian Staub, SARAH 4: A tool for (not only SUSY) model builders, Comput. Phys. Commun. **185,** 1773 (2014).

[75] Emanuele Bagnaschi *et al.*, MSSM Higgs boson searches at the LHC: Benchmark scenarios for run 2 and beyond, Eur. Phys. J. C **79,** 617 (2019).

[76] P. Drechsel, G. Moortgat-Pick, and G. Weiglein, Prospects for direct searches for light Higgs bosons at the ILC with 250 GeV, Eur. Phys. J. C **80,** 922 (2020).

[77] Yan Wang, Jenny List, and Mikael Berggren, Search for light scalars produced in association with muon pairs for $\sqrt{s} = 250$ GeV at the ILC, in *Proceedings of the International Workshop on Future Linear Collider* (2018), arXiv:1801.08164.

[78] Yan Wang, Mikael Berggren, and Jenny List, ILD benchmark: Search for extra scalars produced in association with a Z boson at $\sqrt{s} = 500$ GeV, Report No. ILD-PHYS-PUB-2019-011 (2020), arXiv:2005.06265.

[79] G. Abbiendi *et al.*, Decay mode independent searches for new scalar bosons with the OPAL detector at LEP, Eur. Phys. J. C **27,** 311 (2003).

[80] ATLAS, Combined measurements of Higgs boson production and decay using up to 80 fb^{-1} of proton–proton collision data at $\sqrt{s} = 13$ TeV collected with the ATLAS experiment, Report No. ATLAS-CONF-2018-031, ATLAS-CONF-2018-031 (2018).

[81] Albert M Sirunyan *et al.*, Combined measurements of Higgs boson couplings in proton-proton collisions at $\sqrt{s} = 13$TeV, Eur. Phys. J. C **79,** 421 (2019).

[82] M. Cepeda *et al.*, Report from Working Group 2: Higgs physics at the HL-LHC and HE-LHC, CERN Yellow Rep. Monogr. **7,** 221 (2019).

[83] Philip Bambade *et al.*, The International Linear Collider: A global Project (2019), arXiv:1903.01629.

[84] D. de Florian *et al.*, Handbook of LHC Higgs Cross Sections: 4. Deciphering the Nature of the Higgs Sector, Report No. CERN-2017-002-M, CERN-2017-002 (2016), arXiv:1610.07922.

[85] Tim Barklow, Keisuke Fujii, Sunghoon Jung, Robert Karl, Jenny List, Tomohisa Ogawa, Michael E. Peskin, and Junping Tian, Improved formalism for precision Higgs coupling fits, Phys. Rev. D **97,** 053003 (2018).

[86] Sally Dawson *et al.*, Working Group Report: Higgs boson, in *Community Summer Study 2013: Snowmass on the Mississippi* (2013), arXiv:1310.8361.

[87] S. Heinemeyer and C. Schappacher, Neutral Higgs boson production at e^+e^- colliders in the complex MSSM: A full one-loop analysis, Eur. Phys. J. C **76,** 220 (2016).